CORE
Metadata, citation and similar papers at core.ac.uk
Provided by University of Liverpool Repository

Ge interface engineering using ultra-thin La_2O_3 and Y_2O_3 films: A study into the effect of deposition temperature

I.Z. Mitrovic, [a),1] M. Althobaiti,[2] A.D. Weerakkody[1], V.R. Dhanak[2], W.M. Linhart[2], T.D. Veal[2], N. Sedghi[1], S. Hall[1]

[1]*University of Liverpool, Department of Electrical Engineering & Electronics, Brownlow Hill, Liverpool L69 3GJ, United Kingdom*

[2]*University of Liverpool, Department of Physics and Stephenson Ihnstitute for Renewable Energy, Liverpool L69 7ZF, United Kingdom*

P.R. Chalker[3]

[3]*University of Liverpool, Department of Engineering, Brownlow Hill, Liverpool L69 3GH, UK*

D. Tsoutsou[4], A. Dimoulas[4]

[4]*NCSR Demokritos, MBE Laboratory, Institute of Materials Science, 153 10 Athens, Greece*

Abstract

A study into the optimal deposition temperature for ultra-thin La_2O_3/Ge and Y_2O_3/Ge gate stacks has been conducted in this paper with the aim to tailor the interfacial layer for effective passivation of the Ge interface. A detailed comparison between the two lanthanide oxides (La_2O_3 and Y_2O_3) in terms of band line-up, interfacial features and reactivity to Ge using medium energy ion scattering, vacuum ultra-violet variable angle spectroscopic ellipsometry (VUV-VASE), X-ray photoelectron spectroscopy and X-ray diffraction, is shown. La_2O_3 has been found to be more reactive to Ge than Y_2O_3, forming $LaGeO_x$ and a Ge sub-oxide at the interface for all deposition temperature studied, in the range from 44°C to 400°C. In contrast, Y_2O_3/Ge deposited at 400°C allows for an ultra-thin GeO_2 layer at the interface, which can be eliminated during annealing at temperatures higher than 525°C leaving a pristine $YGeO_x$/Ge interface. The Y_2O_3/Ge gate stack deposited at lower temperature shows a sub-band gap absorption feature fitted to an Urbach tail of energy 1.1 eV. The latter correlates to a sub-stoichiometric germanium oxide layer at the interface. The optical band gap for the Y_2O_3/Ge stacks has been estimated to be 5.7 ± 0.1 eV from Tauc-Lorentz modelling of VUV-VASE experimental data. For the optimal deposition temperature (400°C), the Y_2O_3/Ge stack exhibits a higher conduction band offset (> 2.3 eV) than the La_2O_3/Ge (~ 2 eV), has a larger band gap (by about 0.3 eV), a germanium sub-oxide free interface, and leakage current (~ 10^{-7} A/cm^2 at 1 V) five orders of magnitude lower than the respective La_2O_3/Ge stack. Our study strongly points to the superiority of the Y_2O_3/Ge system for germanium interface engineering to achieve high performance Ge CMOS.

[a)]Author to whom correspondence should be addressed. Electronic mail: ivona@liverpool.ac.uk

I. INTRODUCTION

The most recent studies[1,2] strongly advocate that high performance Ge CMOS (Complementary Metal Oxide Semiconductor) technology is feasible. This technology is attractive due to the Ge intrinsic high mobilities for electrons (3900 cm^2/Vs) and holes (1900 cm^2/Vs) as well as the CMOS compactness (Ge-based n- and p-channel MOSFETs). The smaller band gap of Ge (0.67 eV) has the potential for lower contact resistances compared to Si, and is consequently more suitable for voltage scaling[3]. Sub-nm equivalent oxide thickness (EOT) gate stacks are required to keep the intrinsically high performance of Ge. The focus is on finding suitable high permittivity (κ) dielectric (κ > 20) to form a gate stack with low interface state density and EOT. The most perilous issue is engineering a high-quality interface between Ge and the high-κ dielectric, that is, passivation of the Ge surface. An interfacial layer (IL) either intentionally or unintentionally formed during the high-κ dielectrics deposition process is usually necessary for achieving high electrical performance of Ge-based MOS devices[4-6] but its presence has a significant effect on achieving the desired EOT; it must be as thin as possible and preferably with as high a permittivity as can be achieved. The four most commonly used approaches[7] for forming thin ILs for Ge passivation are: (i) nitridation, (ii) Si-based schemes, (iii) S-based passivation and (iv) GeO_x ($x \leq 2$) grown through thermal, ozone- or plasma-assisted oxidation. The peak electron mobility has been dramatically improved in Ge n-channel MOSFETs over recent years[2,8-12]. The highest reported electron mobility is now approaching 2000 cm^2/Vs[8-9,12]. The key to this achievement has been mainly in interface state reduction at the GeO_2/Ge interface. Thermally grown GeO_2 is the most natural choice[13-18]. A high-quality GeO_2 IL provides a possibility for both p- and n-type Ge channel FETs. However, it is worth recalling that GeO_2 has high water solubility, low desorption temperature (~ 430°C) and low dielectric constant of ~ 6. A detrimental Ge sub-oxide transition layer at a GeO_2/Ge interface can be expected[19,20]. Toriumi's group has systematically investigated[8-11,21-22] the GeO_2/Ge interface in terms of both thermodynamics and kinetics of the Ge oxidation process. An extremely low density of interface states ($D_{it} = 6\times10^{10}$ $eV^{-1}cm^{-2}$) has been reported for relatively thick (~ 20 nm) GeO_2/Ge[23] allowing for high performance Ge n-MOSFETs[21]; note that the high density of the acceptor-type interface states has been found to degrade Ge n-MOSFET performance[18], while it is not a concern for Ge p-MOSFETs due to the position of the charge neutrality level in Ge. An apparent degradation of drive current has been observed when the GeO_2 thickness has been further reduced[3]. A reduction in electron mobility to 265 $cm^2V^{-1}s^{-1}$ has been reported when the GeO_2 IL is ~ 1.2 nm[24]. Oxygen plasma treatment has been proposed to form good quality ~ 5 nm GeO_2/Ge interface at low substrate temperatures, due to the highly reactive O radicals[25,26], leading to demonstration of an extremely low midgap D_{it} of 4.5×10^{10} $eV^{-1}cm^{-2}$. High-pressure oxidation and low temperature oxygen annealing have recently been suggested as the process recipes for nearly ideal GeO_2/Ge system[8]. It seems that low temperature oxygen annealing can work for repairing the dangling bonds in GeO_2/Ge, while high-pressure oxidation suppresses the GeO_x desorption at higher temperature[27], resulting in robust and dense GeO_2 on Ge.

For aggressive oxide scaling with EOT well below 1 nm, the combination of higher-κ oxide and ultra-thin GeO_2 is required. A small amount of rare-earth (RE) metal introduction into the GeO_2 interface layer has been shown to dramatically improve the interface[8]. Rare earth metal ions in oxides generally have large polarizability[28]; among them, La^{+3} has one of the largest values, in excess of 6 Å. This significantly modifies the chemical

bonding at the interface with Ge, redistributing the electronic charge and reducing the electrical activity of the interface states to produce good passivating properties[29]. Rare earth oxides (La_2O_3, Y_2O_3, $LaLuO_3$, Dy_2O_3, Gd_2O_3, CeO_2) react strongly with the substrate resulting in catalytic oxidation of Ge and the spontaneous formation of stable interfacial layers[29-32]. This high reactivity of Ge with high-κ oxide suggests the possibility of GeO_x-free gate stacks. Another passivation route is to introduce a robust, ultra-thin high-k IL barrier, such as Al_2O_3[1,33-37] or Tm_2O_3[38,39]. It is worth noting here that the Ge surface passivated with Al_2O_3 is slowly oxidized without causing GeO_x diffusion or desorption. As a result, all the Ge atoms near the interface are terminated with oxygen atoms or Ge atoms without any dangling bonds under the oxidation condition lower than 4+, leading to low D_{it} even with GeO_x IL. Peak electron and hole mobilities of 689 cm^2/Vs and 546 cm^2/Vs respectively at EOT = 0.76 nm have been achieved by this approach for $HfO_2/Al_2O_3/GeO_x$/Ge gate stack[1].

This paper focuses on the former Ge interface engineering approach using La_2O_3 and Y_2O_3 RE-oxides. These high-κ oxides have moderate reactivity with Ge[40] to form a germanate interface whose purpose is two-fold: firstly to reduce the interface defects and secondly to suppress the GeO_x desorption at the interface. GeO_x-free gate stacks constitute another advantage of this approach by choosing appropriate deposition conditions and annealing procedures[2]. La_2O_3/Ge gate stacks have been investigated by a number of research groups[41-49]. It has been shown[48] that La changes the surface chemistry so that a stable $LaGeO_x$ compound is favoured against the competing reaction of GeO_2 with Ge, resulting in suppression of GeO_x[49]. The stable La–O–Ge bond at the Ge interface provides a surface-state "free" Ge band gap due to the fourfold coordination of La in the GeO_x matrix as predicted theoretically by Houssa et al.[19] This allows for a gate stack with a low density of interface states (~ 10^{11} $eV^{-1}cm^{-2}$) with nearly ideal electrical characteristics[44,47]. Moreover, internal photoemission (IPE) experiments on ZrO_2/La_2O_3/Ge MIS structures[50] have indicated a sufficiently large conduction band offset (CBO > 2 eV). Theoretical calculations using charge neutrality levels predict a $LaGeO_x$ band gap of 5 eV, valence band offset (VBO) of 3 eV[51], and CBO of La_2O_3 and Y_2O_3 on Ge of 2.56 eV[52,53]. The relative permittivity ranges from 9-12[44,54]. It is worth mentioning that only La_2O_3 is reactive to water due to its electropositive nature[55,56] and may thus pose a challenge to the integration into a CMOS process flow. Moreover, LaO_x ($x < 1.5$) is only suitable for nFETs, because LaO_x leads to an interfacial dipole in the gate stack[57]. Passivation of Ge by La_2O_3 subsequently capped with ZrO_2 results in stabilization of the tetragonal crystalline ZrO_2 phase[47,58]. The scaling potential of ZrO_2/La_2O_3/Ge stacks to EOT values as low as 0.5 nm[59] and 0.96 nm[60] has been reported. The La_2O_3 deposition temperature has been found to have a noticeable effect on the capacitance voltage (CV) characteristics[44]. The improved La_2O_3 electrical behaviour is obtained either by depositing the material at higher temperature or by applying post-deposition annealing independent of ambient (H_2, N_2, O_2). The best characteristics (especially low D_{it}) have been obtained when these two conditions are combined, although an increase in both leakage current and EOT has been observed[44]. There has been no explanation of these observations from the structural and band line-up studies, and we address these issues in this paper.

By contrast, Y_2O_3 is Ge-friendly and robust against water. An amorphous Y_2O_3 layer provides a wide bandgap (~ 5.5-5.7 eV)[56], high crystallization temperature (~ 2325°C), relatively high dielectric constant (~ 11–18)[8,61-62] and can effectively passivate the Ge surface without the presence of GeO_x[62,63]. The absence of GeO_x has been

attributed to the stability of the Y_2O_3 interlayer in contact with the Ge substrate[64]. The mechanism for this stability lies in the barrier role of the Y_2O_3 interlayer, which effectively blocks the inter-diffusion of Ge, thus suppressing the growth of unstable GeO_x and so improving the interface quality. Moreover, yttrium can also be used to tune the overall effective work function of the gate stack through the formation of interface dipoles[65]. An electron mobility of 1480 cm^2/Vs for Y_2O_3/Ge n-MISFET has been demonstrated recently[8]. From XPS measurements, the VBO of Y_2O_3/Ge has been found to be 2.78 eV and the band gap, 5.7 eV[66]. Formation of the $YGeO_x$ affects leakage current, hysteresis, interface trap density, and other reliability issues that are important for device operation[9,40,61-62,66-67]. The passivation effect of a $YGeO_x$ IL has been explained by so-called "valency passivation"[9]; the introduction of yttrium atoms effectively suppresses the dangling bonds in the interfacial region and consequently improves D_{it} in the range of 10^{11} $cm^{-2}eV^{-1}$ due to the trivalent RE nature of Y[68-69].

Less is known, however, about the band line-up and structure of bulk and interfacial $LaGeO_x$ and $YGeO_x$ as a function of deposition temperature, which is the main focus of this paper. A systematic study of the structural properties of La_2O_3/Ge and Y_2O_3/Ge gate stacks as a function of deposition temperature has been conducted by Medium Energy Ion Scattering (MEIS), X-ray Photoelectron Spectroscopy (XPS), Vacuum Ultra Violet Variable Angle Spectroscopic Ellipsometry (VUV-VASE), and X-ray diffraction (XRD). The most significant findings from the results which will be presented here are two-fold: firstly, evidence for the optimal deposition temperature to tailor the interfacial layer for effective passivation of Ge interface; secondly, a comprehensive comparison between the two lanthanide oxides (La_2O_3 and Y_2O_3) in terms of band line-up, interfacial features and reactivity to Ge which points to the superiority of the gate stack for adoption in CMOS engineering.

II. EXPERIMENTAL

The 2 nm (nominal) La_2O_3/Ge and 5 nm (nominal) Y_2O_3/Ge gate stacks were deposited by Molecular Beam Epitaxy (MBE) at temperatures ranging from 44°C to 400°C on n- and p-type Ge substrates. Prior to deposition, the Ge surface was cleaned by a mild degreasing with trichloroethylene, acetone and methanol for 5 minutes in each solvent to remove the organics. Then the GeO_x native oxide was thermally desorbed in-situ, by annealing at 450 – 500°C for 30 minutes. The La_2O_3 films deposited at 44°C and 250°C were subjected to post-deposition oxygen (O_2) anneal at 300°C for 15 minutes. Y_2O_3 films were prepared by co-deposition of Y and atomic oxygen at temperatures 225°C and 400°C. The reference samples for spectroscopic ellipsometry and XPS studies entailed a selection of thermally grown GeO_2/Ge with/without capping Al_2O_3 layers, Al_2O_3/Ge as well as oxidized La and Y foils. The GeO_2 films of two nominal thicknesses 4.5 and 12 nm were prepared by ex-situ furnace anneal at 450°C for 5 min and 60 minutes respectively. The capping Al_2O_3 layers with 4 nm nominal thickness were prepared in-situ by co-deposition of Al and atomic oxygen.

The X-ray photoelectron spectra for La_2O_3/Ge stacks were recorded at the Daresbury NCESS facility using an ESCA300 spectrometer with monochromatised Al Kα X-rays of energy 1486.6 eV and electron take-off angles (TOA) of 15-90°. The spectrometer was calibrated so that the Ag $3d_{5/2}$ photoelectron line had a binding energy (BE) of 368.35 eV, and a full width at half maximum (FWHM) of 0.5 eV. The X-ray source power was 2.8 kW

and the spectrometer pass energy was 150 eV with the entrance-slit width of the hemispherical analyzer set to 1.9 mm. Under these conditions, the overall spectrometer resolution was ~ 0.5 eV[70]. Charge compensation was achieved using a VG Scienta FG300 low energy electron flood gun with the gun settings adjusted for optimal spectral resolution. The electron BEs were then corrected by setting the C 1s peak in the spectra (due to stray carbon impurities) at 284.6 eV for all samples[71]. Wide scans were recorded in the 0-1250 eV energy range to determine the elements present in the samples and to check for surface contamination. Then the O 1s, Ge 3d, La 4d, and valence photoelectron lines were recorded separately. The core-level positions are defined as the FWHM and determined to within 0.05 eV by fitting a Voigt curve to the measured peaks. A Shirley-type background[72] is used during the fitting of all the spectra. The angle resolved (AR)-XPS and measurements of Y_2O_3/Ge stacks were made in a separate ultra high vacuum system consisting of an Al Kα X-ray source and a PSP Vacuum Technology electron energy analyzer. This spectrometer was operated with an overall resolution of about 0.8 eV. To diminish the effect of differential charging on evaluating valence band offset[73-75], during the XPS measurements the X-ray beam exposure was across the whole sample. The individual core level scans were performed for the duration of at least an hour until the point at which they reached constant binding energies, and the samples could be considered as charge saturated. Medium energy ion scattering was carried out at the STFC Daresbury Laboratory, with a 100 keV He^+ beam and a double alignment scattering configuration with a scattering angles of 90° and 135°.

The VUV-VASE measurements were performed using a spectral range from 0.5 – 8.8 eV (referring to wavelength range λ = 140-2500 nm), and angles of incidence of 55-75°, by 10° as a step, to maximize the accuracy. The entire optical path was enclosed inside a dry nitrogen purge to eliminate absorption from ambient water vapour and oxygen. The XRD measurements were done using the Philips Xpert XRD system. Electrical characterization was carried out at room temperature on metal insulator semiconductor (MIS) capacitors patterned by Pt e-beam evaporation on the dielectric surface through a shadow mask consisted of circular dots 300 μm in diameter. The back Ohmic contact was made using eutectic In-Ga alloy. The high frequency capacitance voltage data were obtained with a HP4284 precision LCR meter.

III. RESULTS AND DISCUSSION

A. La_2O_3/Ge gate stacks

MEIS and XPS measurements were performed to assess the thickness, distribution of elements and interfacial composition of the ultra-thin La_2O_3/Ge gate stacks. The key findings are outlined in this section. Note that as the thicknesses were less than 5 nm, the results from spectro-ellipsometry on these stacks were not conclusive, hence MEIS results were used. The MEIS energy spectra for the La_2O_3/Ge deposited at 44°C and 400°C are shown in Fig. 1(a). There is a small high energy tail on the Ge signal for sample deposited at 400°C that indicates an inclusion of Ge in the La_2O_3 film. The elemental depth profiles were calculated assuming the lanthanum signal is La_2O_3 with a stopping power density of 6.5 g/cm^3. The calculated La and Ge depth profiles are shown in Fig. 1(b), and reveal the structures of 3 nm La_2O_3/2.2 nm IL/Ge and 2.6 nm La_2O_3/1.7 nm IL/Ge for the stacks deposited at 44°C and 400°C respectively (Table I). A reduction of overall dielectric thickness of

~ 9 Å for the gate stack deposited at higher temperature is evident. Note also a significantly broader edge to the Ge substrate for the layer deposited at 44°C, however a slightly narrower La_2O_3/Ge interface in comparison to the sample deposited at 400°C. The concentration of Ge (10-20%) in La_2O_3 sample deposited at 400°C drops off towards the surface. The results strongly point to the formation of Ge-rich interfacial layers. In the case of 44°C deposited sample, the top layer is La_2O_3, while strong intermixing (penetration of Ge) is visible for sample deposited at higher temperature. It seems that bi-layer structure exists for the 44°C deposited sample, with germanate likely to be present at the interface. This observation is further underpinned by findings from the XPS data.

It has been shown that La is strongly electropositive and tends to strongly attract neighbouring O atoms[49]. The influence of La is considered to regulate the distribution of O in such a way that oxygen density is maximized in the final compound[48]. Furthermore, La on Ge in the presence of oxygen has been found to produce only La–O bonds[19], with no gap states, and the formation of stable $LaGeO_x$ layers[44,47-49]. A penetration of Ge into the La_2O_3 layer observed in this work for the highest deposition temperature, is in agreement with the previous study[44] by energy dispersive X-ray spectroscopy where $LaGeO_x$ layer has been formed across the entire film at the temperature of 360°C.

Fig. 2(a) shows the Ge 3d core level spectra for the 44°C, 250°C and 400°C deposited stacks. The data were fitted using a doublet of Voigt functions corresponding to Ge $3d_{5/2}$ and Ge $3d_{3/2}$ components. The spin-orbit splitting and area ratio values of 0.6 eV and 2:3 were fixed for the fit. The spin-orbital splitting for Ge 3d substrate peak (Ge $3d^0$) can be seen in Fig. 1(a) at energies of 28.6 and 29.2 eV. No presence of GeO_2 at the interface for La_2O_3/Ge stacks is evident from the Ge 3d core level spectra (see the reference GeO_2/Ge spectrum at the bottom of Fig. 2(a) for comparison); the Ge 4+ oxidation state has been reported to occur above 3 eV; @ 3.2 eV[49,76] and 3.4 eV[77,78] from the Ge $3d^0$. Considering that the Gibbs free energy of formation of GeO_2 (–387 kJ/mol at 1000°K), the GeO_2 is thermodynamically unstable so that a GeO_2 layer is unlikely to form at the La_2O_3/Ge interface. Taking into account the electronegativity of Ge (2.01 using Pauling's scale), $LaGeO_x$ is expected to appear between the chemical shifts of GeO (Ge^{+2}) and Ge_2O_3 (Ge^{+3}), i.e. between 1.7 eV and 2.8 eV[17,77]. The energy shift of 2.2 eV for $LaGeO_x$ has been reported[48,49]. In our work, the presence of $LaGeO_x$ (3/2 and 5/2) can be de-convoluted from the spectra at the chemical shift of +2.5 to +2.6 eV. Further evidence of $LaGeO_x$ formation comes from the observed shift of La $4d_{5/2}$ doublet peak in Fig. 3(a) towards the higher BE (~ 0.1-0.2 eV) in comparison to the pure La_2O_3 at 102.2 eV[79]. Note that the BE of La $4d_{5/2}$ for the 44°C deposited sample shows no shift in comparison to the pure La_2O_3, substantiating the MEIS result in Fig. 1(b) that this layer consists mainly of lanthanum oxide. The O 1s spectrum shows further evidence of a clear La-O bond at 528.6 eV[79] (see top graph in Fig. 3(b)), which flattens out as the deposition temperature increases, and the centroid peak shifts towards lower binding energies for the 400°C deposited sample consistent with a formation of $LaGeO_x$ film[44].

The Ge 3d spectra in Fig 2(a) confirm the existence of an interfacial layer ascribed to GeO_x as the binding energy shift lies at ~ 1.7 eV from the Ge $3d^0$. The reported values of Ge^{+1} and Ge^{+2} are at ~ 1 eV and 1.8 eV shifts respectively[77,78]. The spin-orbit splitting for GeO_x could only be resolved in the 44°C sample (see inset in

Fig. 2(a)), while for higher deposition temperatures, the fitting shows only a very small single peak. The angle-resolved XPS of this region for the 400°C deposited La_2O_3/Ge is shown in Fig. 2(b); the peak is more pronounced as the angle is increased indicating that GeO_x is present at the interface but surprisingly also in the oxide bulk. The same finding can be deduced from the AR-XPS spectra of O 1s core level shown in the inset of Fig. 3(a). As the angle is increased, the broad centroid peak is transformed, showing sub-peaks as a signature of La-O-La, La-O-Ge, La-OH and the Ge-O-Ge bonds. The surface and even bulk hydration has been found to take place for all binary lanthanide oxides[41,79,80], and its strong presence is visible for these samples too.

The band diagram of the La_2O_3/Ge stack deposited at 400°C was derived using the valence[81,82] and O1s energy loss XPS spectra[83,84] and is shown in Fig. 4. The high resolution valence band (VB) spectra for the three La_2O_3/Ge stacks are plotted in Fig. 4(a). Although the accuracy in the determination of the Ge VB maximum is quite limited, we measure a VBO value of 2.75 ± 0.15 eV for 400°C deposited sample, in reasonable agreement with the theoretically predicted value of 3.0 eV for La_2GeO_5 and $La_2Ge_2O_7$ compounds[57]. The band gap is usually obtained from the inelastic energy loss features observed on the high binding energy side of the core level photoemission peaks[79,82,84]. The band gap equals the energy distance between the photoemission peak centroid and the onset of the features due to single particle excitations[83]. Fig. 4(b) shows the energy loss features of the O 1s peak for the 400°C deposited sample. The band gap of the $LaGeO_x$ film was determined to be 5.45 ± 0.2 eV. By taking into account the band gap of Ge of 0.67 eV, the calculated CBO for $LaGeO_x$/Ge is about 2 eV (Fig. 4(c)). This is in agreement with the IPE study on ZrO_2/La_2O_3/Ge film which indicates CBO of interfacial $LaGeO_x$ film of > 2.0 eV[50]. It is worth noting that the valence band edge of La_2O_3 films reduces by about 0.5 eV as the deposition temperature decreases from 400°C to 44°C as can be seen from Fig. 4(a). This observation might indicate structurally different multi-layer stacks; in particular for the 44°C sample, where the MEIS results point to predominantly La_2O_3 layer on top. For the latter, this implies a VBO of 2.25 ± 0.15 eV and hence conduction band offset value for La_2O_3 on Ge of ~ 2.6 eV from our work, in close agreement with theoretically predicted CBO value of 2.56 eV[52,53]. It has been observed that La_2O_3 reacts strongly with Ge substrate to form spontaneously a nearly uniform $LaGeO_x$ compound across the entire film thickness during deposition[47-49]. It is evident from the XPS Ge 3d core level spectra in Fig. 2 that $LaGeO_x$ is indeed formed at all deposition temperatures in this study. However, our results do not show a uniform layer across the whole thickness of the gate stack. This is particularly evident at lower temperatures. Furthermore, the noticeable shift in the valence band offset in Fig. 4(a) cannot be explained by the formation of a structurally different germanate layer formed at a different deposition temperature. Theoretical work points to the band gap and band offsets of the La germinates to be relatively independent of Ge content, because the valence band top is formed of O 2p states and the conduction band bottom is formed of La 4d states, which do not change with composition[51]. The theoretically predicted values of band gap and valence band offsets are 5.0 eV and 3.0 eV respectively for both $La_2Ge_2O_7$ and La_2GeO_5[51]. However, the observed band line-up substantiates the structural observation from MEIS on transition from a bi-layer La_2O_3/$LaGeO_x$ at 44°C to predominantly $LaGeO_x$/Ge gate stack at 400°C. A further argument which underpins our band line-up results, is the observation from electrical measurements[44] that the stack with the best passivation efficiency, that is the lowest $D_{it} < 9\times10^{11}$ $eV^{-1}cm^{-2}$, has been obtained at the highest deposition temperature (360°C); however with higher leakage current and lower scalability in comparison to the La_2O_3/Ge deposited at lower temperatures (44 - 225°C). Interface state density D_{it} ($eV^{-1}cm^{-2}$)

for as-deposited La_2O_3/Ge stacks has been reported to be < 9×10^{11}, 1.4×10^{12}, 3×10^{12} and 4×10^{12} for samples deposited at 360°C, 225°C, 150°C and room temperature (44°C) respectively[44].

In summary of this section, our structural study on MBE-deposited La_2O_3/Ge gate stacks shows that as the deposition temperature increases, the stack converts towards a uniform $LaGeO_x$ layer which is beneficial for passivation of the Ge surface. However, the conduction band offset drops by ~ 0.5 eV causing higher leakage, leads to a permittivity reduction to ~ 12[44] and hence lowers the scalability. Moreover, our study confirms that La_2O_3 reacts strongly with Ge and removes the GeO_2 completely. This could allow an abrupt $LaGeO_x$/Ge interface, introducing remote phonon and Coulombic scattering centers directly on the channel and so reducing carrier mobility[57].

B. Y_2O_3/Ge and Al_2O_3/Ge gate stacks

This section presents a detailed VUV-VASE study of Y_2O_3/Ge stacks deposited at two different temperatures (225°C and 400°C) with a special emphasis on determining the dielectric function and absorption coefficient spectra, as well as estimating the band gap and sub-band gap absorption features. The interfacial composition, band line-up and crystallinity were ascertained from XPS and XRD measurements. In addition, the effect of Al_2O_3 as a capping layer was studied.

B.1. Thickness, band gap and sub-band gap absorption

Spectroscopic ellipsometry is very sensitive to the presence of surface layers in the order of just a fraction of a nanometer. The primary sensitivity comes from changes in phase, i.e. ellipsometric angle Δ. Due to the high energy range of SE measurements in this study, all dielectric films became absorbing. The UV absorption is often modelled using a Tauc-Lorentz dispersion relationship[85]. The overall absorption shape is described by an amplitude, broadening, center energy, and band gap energy. The index of refraction is determined from both the Kramers-Kronig (KK)[86] transformation of imaginary part of dielectric function along with addition of an offset and UV pole to account for absorption that is outside the measurement spectral range. The modelling and fitting procedure in this study consisted of firstly, determining the thickness and optical constants in non-absorbing (transparent) region of spectra from 0.5–6 eV using a Cauchy layer representative of a dielectric film. Then, a Kramers-Kronig consistent B-spline layer[87] was used to extend the optical constants into the higher energy range, up to 8.5 eV. This method is consistent with the point-by-point fit method[88] used in WVASE32, but with two added advantages: firstly the layer maintains KK consistency which forces the optical constants to keep a physical shape, secondly the optical constants remain smooth and continuous over the full spectrum, with a controllable parameter to decide the resolution of points. Additionally, the B-spline layer was replaced with the general oscillator model with a possibility of using Cody-Lorentz and Tauc-Lorentz oscillators to discern possible sub-band gap absorption features in the gate stacks and to determine the band gap.

Optical constants for germanium are available in the literature up to 6 eV photon energy range. We used this spectral range to fit the surface layer thickness of native GeO_2 for the reference Ge substrate. Initial

measurements (upon opening the container in N_2 purged environment) on a Ge substrate gave a GeO_2 native oxide thickness of 2.93 nm. Then the germanium optical constants were fitted using a Kramers-Kronig consistent B-spline layer over the entire spectral range. This sample was used as a reference Ge substrate layer to determine the optical constants of thermally grown GeO_2 as well as Y_2O_3 and Al_2O_3 films. The thickness values of the stacks are summarized in Table I. It can be seen that the thickness of Y_2O_3 films is ~ 6-8 nm, and of Al_2O_3 ~ 8-9 nm. The reference thermally grown GeO_2 layers have thicknesses of 4.4 nm (non-capped) and 3.2 and 7.2 nm for Al_2O_3 capped samples. The mean squared error between the experimental and theoretical curves was in all cases below 5, consistent with a good quality fit of the data.

The real and imaginary part of dielectric function vs photon energy (E) for the stacks is shown in Figs. 5(a) and (b) respectively. A pronounced absorption below the band edge can be observed for the Y_2O_3/Ge sample deposited at 225°C, and this is visible in the energy range from about 4 to 5.5 eV in both real and imaginary parts of the dielectric function spectra (see top graphs in Figs. 5(a) and (b)). The band-edge tailing is much less apparent for the Y_2O_3/Ge deposited at higher temperature of 400°C. For comparison of these spectra, in the bottom parts of Figs. 5(a) and (b), the real (ε_1) and imaginary (ε_2) parts of dielectric function for GeO_2/Ge samples, both non-capped and Al_2O_3 capped, are plotted as a reference. The sub-band gap features are evident for GeO_2/Ge samples and this region correlates with the pronounced absorption for the Y_2O_3/Ge sample deposited at 225°C. For the reference GeO_2/Ge sample in this work, a peak appears at ~ 5 eV, while in Ref. 39, two peaks are visible, at 4.4 eV (due to Ge) and at 5.1 eV. Toriumi et al.[89] have reported a peak at 5.1 eV for the GeO_2/Ge sample, thought to be associated with neutral O vacancies or Ge^{+2} in oxygen deficient GeO_2[90]. The high-level ab-initio calculations[91,92] have shown that –GeX_3 (E′ center @ 5.06 eV[90]) and X_3Ge-GeX_2 (E′-oxygen vacancy @ 5.16 eV[90]) defects are able to form a broad absorption band near 5 eV. Note that X refers to –OH and -$OGeH_3$ simulating the :Ge< defect[92]. From the data in Fig. 5(b) it is evident that the pronounced sub-band gap absorption for Y_2O_3/Ge sample deposited at 225°C compares to the absorption features in the GeO_2/Ge spectra and could indicate a possible defective non-stoichiometric germanium oxide interfacial layer. Such an interfacial layer is not apparent for the sample deposited at 400°C.

Following the extraction of the dielectric function ($\tilde{\varepsilon} = \varepsilon_1 + j\varepsilon_2$) for the Y_2O_3, Al_2O_3 and GeO_2 films using the methodology above, the ε_1 and ε_2 parameters are converted into refractive index (n) and extinction coefficient (k) using the KK relations. The absorption coefficient (α) can be found from the extinction coefficient as

$$\alpha = \frac{4\pi k(E)E}{hc} \qquad (1)$$

where h is the Planck's constant, c is the speed of light and E is the photon energy. The band gap in this work is extracted from the Tauc-Lorentz model[85] and α-method. The functional form of the Tauc-Lorentz model and its simplified expression[93,94] are given in the Appendix. The plots of α vs E for Y_2O_3 and Al_2O_3 films are shown in Figs. 6(a) and (c) respectively. The associated Tauc-Lorentz plots are depicted in Figs. 6(b) and (d). The linear

extrapolation of the segments on the curves in the non-absorbing regions gives the band gap values of 5.99 eV for Y_2O_3 layers, and 6.43 eV for Al_2O_3 layer from α-method. The associated band gap values from the Tauc-Lorentz plots are ~ 0.3 eV lower than those derived from the α-method. This result is in agreement with the observations in Ref. 95 that the band gap values obtained from the α-method can be by ~ 0.7 eV larger than the ones determined using the Tauc- or Cody-Lorentz methods (see Appendix). In the insets of Figs. 6(b) and (d), the corresponding $(\alpha E)^2$ vs E graphs are added (valid for direct band gap transitions[96]). A summary of the experimental band gap data obtained from this work and literature[39,56,66,97-102] is shown in Table I. It can be seen that the band gap of Y_2O_3 from the Tauc plots is 5.7 ± 0.1 eV for both deposition temperatures. A similar value has been reported for a radio frequency (rf) sputtered Y_2O_3/Ge stack using SE[56] and XPS[66] measurements. The value reported for Y_2O_3 on Si is 5.6 (from SE)[97], on SiO_2 is 6.0 (from XPS)[98], and for single crystal 6.1 eV (from SE)[99].

The Tauc coefficient is found to be 1145.4 $eV^{-1/2}cm^{-1/2}$ for both samples. It has been argued that the Tauc plot is related to the degree of order in the structure[103], i.e. disorder generates defects and hence removes states from the bands and generates band tails of localized states. These band tails are generally described by the Urbach exponential[104]

$$\alpha = \alpha_0 \exp\left(\frac{E}{E_u}\right), \qquad (2)$$

where α_0 is the constant and E_u is the Urbach energy. In a logarithmic plot of the absorption coefficient, the Urbach tail appears as a linear region at energies below the absorption edge. The logarithmic plot of α vs E, in the sub-band gap energy range (< 6 eV) is shown in the inset of Fig. 6(a). An apparent linear region of the plot is visible for the Y_2O_3 sample deposited at 225°C, being indicative of a presence of an Urbach tail. The inverse of this slope gives the Urbach energy of 1.1 eV. The values of E_u = 1.4 eV and the Tauc coefficient of 1344 $eV^{-1/2}cm^{-1/2}$ have been reported for polycrystalline HfO_2 film[103]. A decrease in band tailing for the HfO_2 samples annealed at higher temperatures has been reported and attributed to defect reduction and temperature induced crystallization[105,106]. The amorphous samples have been proposed to have a continuous and more dense bond network and hence a lower density of defects, which is substantiated by the lower trapped charge density[103,107]. In this work, the sample deposited at higher temperature shows no apparent Urbach tail and has less pronounced sub-band gap absorption region. However, there is no shift of the band edge in comparison to 225°C deposited sample (see Fig. 6(a)), indicating a similar structure. This argument is substantiated by the XRD graphs shown in Fig. 7(d), where both films prove to be polycrystalline. The XRD pattern shows polycrystalline phases of Ge (004) plane and Y_2O_3 (631) plane for both samples.

B.2. Interfacial layer study for Y_2O_3/Ge

The Ge 3d XPS core levels can best represent the chemistry at the interface because of their sufficient surface sensitivity and good resolution due to a narrow FWHM[108]. The relevant Ge 3d spectra fitted using a doublet

(due to spin-orbit splitting) Voigt functions for each peak are shown in Fig. 7(a). The Ge $3d^0$ substrate peak is fitted with a doublet of Ge $3d_{5/2}$ (@29.0 eV) and Ge $3d_{3/2}$ (@ 29.6 eV) with spin-orbit splitting of 0.6 eV and intensity ratio of 2:3 respectively. A high BE shoulder to the Ge $3d^0$ substrate peak can be seen for both Y_2O_3 samples, however with a higher intensity for the layer deposited at 400°C (see Fig. 7(a) bottom). Also note that Ge $3d^0$ is less pronounced for the latter due to the thicker dielectric layer for this sample (see Table I, 7.9 nm for 400°C vs 6.3 nm for 225°C deposited sample). The rising edge at a BE lower than ~ 28 eV originates from Y 4p to O 2s peaks at ~ 25 eV. The formation of the interfacial layer will be reflected in the Ge 3d spectra as positive shifts (with respect to the substrate Ge $3d^0$ peak) when Ge reacts to form $YGeO_x$ layer. It has been reported that the Y-Ge-O bonding configuration gives rise to a BE shift within the range of + 2.2 to 2.5 eV due to a second nearest-neighbor effect, which is distinctly different from a O-Ge-O type bonding (+3.4 eV shift)[77,109]. In our spectra in Fig. 7(a), the chemical shift for $YGeO_x$ layer is visible at +2.5 to + 2.7 eV from the substrate peak. Note the difference in the interfacial layer between the two samples. The lower temperature deposited Y_2O_3/Ge stack features GeO_x layer at the interface, with a chemical shift of 1.1 eV consistent with +1 Ge oxidation state[78]. The higher temperature deposited stack has sub-oxide fully eliminated, and GeO_2 appears at the interface.

The Y 3d core level spectra were also measured to study the additional bonding and are shown in Fig. 7(b). The peak appearing at ~156.95 eV for Y_2O_3/Ge samples represents the co-existence of Y_2O_3 at 156.86 eV (see top graph for Y_2O_3 reference in Fig. 7(b)) and Ge–O–Y bonding at 157.28 eV (see middle and bottom part of Fig. 7(b)). In addition, a positive shift from a reference Y_2O_3 bulk value can be seen from the O 1s spectra shown in Fig. 7(c), and this provides firm evidence of charge transfer and formation of $YGeO_x$ at the interface. Note also that both the Y 3d and O 1s spectra show that Y-OH bond from moisture absorption is present, as in the case of La_2O_3/Ge stacks.

The results imply that Y–O–Y bonding configuration near the surface transforms to a Y–O–Ge configuration near the interface due to the incorporation of Ge atoms into the Y_2O_3 matrix. It has been inferred that Y and Ge atoms intermix more significantly at a higher process temperature[68]. The out-diffusion of Ge signifies the breaking of the strong covalent Ge-Ge bonds even at room temperature. The chemical bonding model proposes possible bond weakening via charge transfer during the formation of chemical bonds[110]. Since the electronegativity difference between Y and Ge (1.22 and 2.01 using Pauling's scale) is large, charge transfer and hence the bond weakening can be significant. Room temperature mixing has also been observed for Si, and the concept of metallic screening of covalent bonds has been used to explain the bond weakening[111,112].

In order to study the effect of temperature on the interfacial layer characteristics of Y_2O_3/Ge, XPS in-situ annealing measurements were performed in the temperature range of 425°C to 750°C, with a step of 25°C. The Ge 3d core level spectra as a function of annealing temperature are shown in Fig. 8. A stronger formation and more pronounced $YGeO_x$ shoulder is visible for the Y_2O_3/Ge sample deposited at 400°C. The fitting of the Ge 3d core level at different annealing temperature is performed using the same procedure described above. The relevant graphs for the two Y_2O_3/Ge samples are shown in Figs. 9(a) and (b). The Y_2O_3 sample deposited at 225°C shows less pronounced interfacial layer shoulder, with GeO_x present at all annealing temperature as can

be seen from Fig. 9(a). On the contrary, the 400°C deposited Y_2O_3 sample shows presence of GeO_2 IL layer until the annealing temperature of 525°C. For this gate stack after the 550°C annealing temperature, the interface is pristine $YGeO_x$ layer.

B.3. Estimation of VBO and derivation of a band diagram for Y_2O_3/Ge

According to Kraut's method[113], the valence band offset value for a Y_2O_3/Ge heterojunction can be determined using the following equation

$$VBO = (E_{Ge3d} - E_V)^{Ge} - (E_{Y3d} - E_V)^{Y_2O_3} + \delta_{CL} \qquad (3)$$

where E_{Ge3d} and E_{Y3d} are the binding energies of the Ge 3d and Y 3d core levels that have been selected as references for Ge substrate and Y_2O_3 respectively. Ev refers to the valence band maximum (VBM) for the Ge substrate and bulk reference Y_2O_3 sample and can be estimated from the valence band spectra using linear interpolation method[114]. The term δ_{CL} is defined as the energy difference between the Ge 3d and Y 3d core levels referring to Ge substrate and Y_2O_3 from the interface Y_2O_3/Ge sample, i.e.

$$\delta_{CL} = E_{Ge3d}^{Ge} - E_{Y3d}^{Y_2O_3}.$$

Fig. 10(a) shows the selected core levels and valence band spectra for a clean bare n-Ge substrate (top), for interfacial Y_2O_3/Ge (middle) and for a bulk Y_2O_3 (bottom) films. The energy difference between the Ge 3d 5/2 and the VBM in the bare, pre-clean Ge sample (Fig. 10(a), top) was measured to be 29.41 ± 0.1 eV. This value compares to published results of 29.47 ± 0.07 eV[115], 29.40 ± 0.03 eV[116], 29.30 ± 0.1 eV[117], and 29.61 ± 0.1 eV[39]. The value of δ_{CL} is found to be 127.77 ± 0.1 eV for the Y_2O_3/Ge deposited at 225°C (shown in Fig. 10(a), middle), and 127.85 ± 0.1 eV for the sample deposited at 400°C. The energy difference for the bulk Y_2O_3 reference sample was estimated to be 154.50 ± 0.1 eV. By inserting the estimated values in Eq. (3), the VBO is determined to be 2.68 ± 0.2 eV. The valence band spectra for the two Y_2O_3/Ge stacks are depicted in Fig. 10(b). We measure directly from these graphs VBO values of 2.45 eV and 2.34 eV with an error bar of ± 0.2 eV, for 225°C and 400°C deposited samples respectively. It is worth noting that the VBO value is within the tolerance bar of the measurement for both samples. This is in contrast with the La_2O_3/Ge samples, where a more substantial decrease of the VBO value with the raise of the deposition temperature was observed (see Fig. 4(a)). Note that the spectra shown in Fig. 4(a) are obtained from an instrument with higher spectral resolution than once shown in Fig. 10(b). It is worth mentioning that we have re-measured the core levels (Ge 3d, Y 3d, O 1s) and valence band region for the Y_2O_3/Ge samples using a monochromated XPS instrument, and the result of 2.68 ± 0.2 eV was confirmed using the Kraut method. The full band diagram of Y_2O_3/Ge is drawn in Fig. 10(c) using the Kraut's value of the VBO and the band gap value obtained from the Tauc plots (see section B.1). The conduction band offset (CBO) for Y_2O_3/Ge stack is calculated to be 2.35 eV. The value of the VBO of 2.78 eV has been reported for Y_2O_3/Ge from the Kraut's method in Ref. 66, however the values of the core level

differences in Eq. (3) have not been stated, so direct comparison with our data is not possible. The obtained CBO value of 2.35 eV from this work compares to the theoretically predicted value of 2.56 eV[52,53].

B.4. Electrical characterization of Y_2O_3/Ge stacks

The high frequency capacitance voltage and leakage current density characteristics for a MIS capacitor from the as-deposited Y_2O_3 films grown at 225°C and 400°C, are shown in Figs. 11 and 12, respectively. The CV curves of the 225°C deposited Y_2O_3 sample (Fig. 11(a)) exhibit high frequency dispersion with large bumps in the weak inversion regime. A notable improvement in the CV characteristics is observed as the growth temperature increases from 225°C to 400°C. The aforementioned result could be correlated with the Ge 3d XPS spectra presented in Fig. 7, where full elimination of GeO_x sub-oxide and enhanced $YGeO_x$ formation have been demonstrated in the case of the 400°C-deposited Y_2O_3/Ge stack.

It is evident from Fig. 12 that the leakage current of the 400°C-deposited sample is subsequently kept below 10^{-6} A/cm^2 at 1 V, as opposed to La_2O_3 that suffers from high leakage current of ~ 10^{-1} A/cm^2 at 1 V for samples deposited at 360°C (see Ref. 44). This observation is in good agreement with the band diagrams presented in Figs. 4 and 10, where the Y_2O_3/Ge stack was found to exhibit a higher conduction band offset (> 2.3 eV), than the respective La_2O_3/Ge (~ 2 eV). Furthermore, this behaviour is in good agreement with the reported VASE and XPS spectra of the as-deposited Ge/Y_2O_3 samples (see Figs. 5, 7(a) and 9), where a reduction of defective GeO_x species has been observed at a growth temperature of 400°C.

C. The effect of an Al_2O_3 capping layer

The band gap value of Al_2O_3 layer is found to be 6.1-6.4 from the VUV-VASE results (see Table I and Fig. 6(c)-(d)). The ALD-deposited Al_2O_3 has been reported to have a much lower density (3.1-3.3 g/cm^3) than sapphire, and a lower band gap of ~ 6.2 eV (from photoconductivity measurements)[100,101] and 6.5 eV (from XPS)[102]; for sapphire the band gap is 8.8 eV[53,118]. No Urbach tail was evident for the Al_2O_3/Ge in this work, suggesting a negligible sub-band gap absorption. It has been argued recently that Al_2O_3 is a good oxygen diffusion barrier and therefore blocks the O vacancy diffusion that allows the volatilisation of GeO and the creation of sub-stoichiometric GeO_x interface states[57]. Calculations of electronic structures of interfaces and interface defects and of oxide reactions and considerations of diffusion barrier properties by Robertson's group[57,119] suggest that a thin Al_2O_3 layer in the overall dielectric might be a preferred passivation scheme for Ge channels[34,35]. Furthermore, the difference in the O density between La_2O_3, Y_2O_3 and Al_2O_3 allows for different behaviour of these oxides on Ge[49]. As discussed in the introduction, both La_2O_3 and Y_2O_3 belong to a group of intimate dielectrics on Ge, i.e. they form stable germanate layers in contact with Ge. On the contrary, Al_2O_3 acts as a barrier on Ge. This has further been associated with the cation radius of the corresponding oxides[49]. In particular the large ionic radius of La^{+3} (117 pm) compared to Al^{+3} (67.5 pm), implies large M–O bond length (M - metal ion), and consequently a less dense O structure.

The interfacial features for the selection of GeO_2/Ge with and without Al_2O_3 capping layers can be found from inspecting the Ge 3d core levels, and are shown in Fig. 13. For the non-capped 4.4 nm GeO_2/Ge layer, a strong presence of Ge^{+4} oxidation state is evident from the chemical shift to the Ge $3d^0$ peak of > 3 eV[49,77-78] (Fig. 13(a)). After the Al_2O_3 capping layer deposition on 3.2 nm GeO_2/Ge, the shift to lower binding energy of the IL peak in Fig. 13(b) reveals the impact of Al_2O_3 deposition on the GeO_2 layer. This behaviour suggests the formation of a germanate layer ($AlGeO_x$) at the Al_2O_3/GeO_2 interface. Note also the presence of GeO_x at the interface for this sample. For the thicker 7.2 nm GeO_2 layer with Al_2O_3 cap, only a sub-peak referring to $AlGeO_x$ can be observed from Fig. 13(c). In the case of Al_2O_3/Ge, no high BE shoulder is apparent, rather just a peak referring to the Ge $3d^0$ substrate (Fig. 13(d)) suggesting no IL. Further evidence comes from the Al 2p spectra shown in Fig. 14. The Al 2p spectrum for Al_2O_3/Ge sample exhibits no clear change, suggesting that there is no detectable chemical reaction in the Al_2O_3 capping layer, and that Al_2O_3 acts indeed as a barrier layer. On the contrary, for the Al_2O_3/GeO_2/Ge structures there is a clear shift for both Al 2p and O 1s peaks towards higher BEs in agreement with $AlGeO_x$ formation discussed above. These observations indicate that the Ge in-diffusion through the GeO_2 into the Al_2O_3 and the intermixing between these different layers lead to a $AlGeO_x$ IL formation, possibly more stable than the GeO_2 interlayer[29]. A recent theoretical study predicted that the incorporation of Al into the GeO_2 matrix leads only to the formation of Ge–O–Al bonds, with no defect states inside the Ge bandgap[19], indicating that the formation of the $AlGeO_x$ interlayer should not be detrimental to the interface quality[7,22,34,35].

In summary of this section, there is evidence that Y_2O_3 shows a more moderate reactivity to Ge and shows feasibility for a GeO_2-interfacial layer at the higher deposition temperature of 400°C. The conduction band offset has been derived from the XPS and VUV-VASE data and shows a sufficiently large (~ 2.3 eV) value to allow for the measured low leakage (< 10^{-6} A/cm^2 @ 1 V). The stack transforms into pristine $YGeO_x$/Ge layer, with no GeO_2 IL, for annealing temperature above 525°C. Our experimental results confirm that Al_2O_3 acts as a barrier on Ge, with no detectable IL, within a resolution of the experimental techniques used.

IV. SUMMARY & OUTLOOK

A comprehensive study of ultra-thin La_2O_3/Ge and Y_2O_3/Ge gate stacks prepared by molecular beam epitaxy has been conducted in this paper for consideration as interfacial layers for Ge surface passivation. In particular, the effect of deposition temperature, ranging from 44-400°C, on interfacial features, band line-up, band gap and sub-band gap absorption, and crystallinity has been investigated by MEIS, VUV-VASE, XPS and XRD techniques. Both La_2O_3 and Y_2O_3 show a reactivity to germanium. A strong presence of germanate layers was found from the high binding energy shoulders to the Ge 3d substrate XPS core level peak, with a chemical shifts of +2.5-2.6 eV for $LaGeO_x$, and +2.5-2.7 eV for $YGeO_x$. The higher deposition temperature the higher intensity of the germanate layers formation was evident for both gate stacks. However, the interface structure was found to be somewhat different. In the case of La_2O_3/Ge, there is no GeO_2 present at the interface for all deposition temperatures studied, rather germanium sub-oxide species dominate the interface and even they have been found in the bulk of ultra-thin (2-3 nm) films from angle-resolved XPS data. The high-resolution valence band spectra for the La_2O_3/Ge stacks have shown a noticeable positive (~ 0.5 eV) shift in the valence band edge, as the

deposition temperature increased from 44°C to 400°C. This observation underpins previously reported electrical characterization data that the stack with the best passivation efficiency has a uniform $LaGeO_x$ layer, but with higher leakage current and hence low scalability. The band diagram has been derived for $LaGeO_x$/Ge from the XPS data with values for valence band offset of 2.75 ± 0.15 eV and band gap of 5.45 ± 0.2 eV, in reasonable agreement with recent theoretical calculations.

A Y_2O_3/Ge gate stack deposited at 225°C shows a GeO_x interfacial layer. The VUV-VASE data have enabled extraction of dielectric function and absorption coefficient versus photon energy for the Y_2O_3/Ge stacks. The pronounced sub-band gap absorption region is distinctly evident in the broad region from ~ 4.5-5.5 eV from the imaginary part of dielectric function and absorption coefficient spectra for the 225°C deposited stack. This absorption range could be attributed to a reported neutral oxygen vacancy coordinated with two Ge ions (at 5.06 eV) and/or a Ge^{+2} coordinated with two oxygens (at 5.16 eV) defects; this result substantiates the existence of sub-stoichiometric GeO_x layer. The stack deposited at 400°C has no such absorption region, and GeO_2 interfacial layer has been found from the Ge 3d XPS core level spectra. Furthermore, after the annealing above 525°C, this stack has become GeO_2-free, transforming into pristine $YGeO_x$/Ge layer. The band diagram has been derived for the Y_2O_3/Ge using the Kraut's method for the estimation of VBO (2.68 ± 0.2 eV) and Tauc-Lorentz method for the band gap (5.7 ± 0.1 eV). The band gap of Al_2O_3 has been found to be 6.1-6.4 eV from the Tauc-Lorentz and α-methods. There was no detectable interfacial layer for Al_2O_3/Ge stack, indicating possible barrier role of alumina layer.

A notable improvement in the capacitance voltage and leakage current density characteristics has been observed for the Y_2O_3/Ge stacks as the growth temperature increased from 225°C to 400°C. This result is in agreement with the structural data, as the detrimental effect of GeO_x interfacial layer on electrical properties can be expected for the 225°C deposited stack.

In summary, the results of this study unambiguously point to two important findings: firstly the optimal deposition temperature is in the higher range, at ~ 400°C, as this allows for more uniform germanate layer at the interface with better passivation properties; secondly comparing two rare-earth stacks, La_2O_3/Ge with Y_2O_3/Ge, deposited at the optimal temperature (~ 400°C), the latter is seen to have more attractive features for Ge interface engineering: moderate reactivity to Ge, GeO_x-free interface, higher conduction band offset (~ 2.3 eV), larger band gap (~ 5.7 eV), and lower leakage current (< 10^{-6} A/cm^2 at 1 V). As such, Y_2O_3/Ge is a serious contender for interface engineering in future Ge CMOS technology.

ACKNOWLEDGEMENTS

The work was funded by the EPSRC grant no. EP/1012907/1, United Kingdom. The MEIS measurements were performed courtesy of Dr P. Bailey and Dr T.C.Q. Noakes from the Daresbury Laboratory, UK. The VUV-VASE experiments were done at J.A. Woollam Co. Inc., NE, USA courtesy of J.N. Hilfiker. The authors thank Dr O. Buiu from LOT-Oriel for useful discussions regarding the VASE results; Dr C. Muryn from Chemistry

Department at the University of Manchester, UK for XRD measurements, and Prof C. McConville at University of Warwick, UK for use of monochromated XPS system. One of the authors (MA) acknowledges support from Physics Department, Taif University, Saudi Arabia. Also thanks to P. Spencer from Physics Department, University of Liverpool, UK for performing some of the XPS experiments in this work under the EPSRC 2011 vacation bursary award scheme.

APPENDIX

The band gap can be determined from the spectroscopic ellipsometry data using a linear extrapolation of the threshold of optical absorption from either the extinction coefficient (k) curve, the imaginary part of the dielectric function (ε_2) , the absorption coefficient (α) curve, or plots of the Tauc-Lorentz and Cody-Lorentz[95]. It has been shown[95] that the band gap value determined from the α-method is larger than those determined from the k and ε_2 methods, due to an extra factor of energy gained when converting from k or ε_2 to α. This factor of energy adds an additional concave upwards nature to the absorption coefficient curve, which has the effect of shifting the linearly extrapolated band gap to higher energy. On the contrary, the Tauc and Cody-Lorentz generate smaller band gap values due to the fact that it uses the square root of the imaginary part of the dielectric function, which decreases the concave upwards nature of the spectrum.

The functional form of the Tauc-Lorentz model[85] is given as

$$\begin{aligned}\varepsilon_2(E) &= \frac{A_T(E-E_g)^2}{E^2}\frac{A_L E_0 CE}{(E^2-E_0^2)^2+C^2E^2} \\ &= \frac{1}{E}\frac{AE_0C(E-E_g)^2}{(E^2-E_0^2)^2+C^2E^2}\end{aligned}, \qquad (A.1)$$

where A is the transition amplitude, C is the broadening coefficient of the Lorentz oscillator, E_0 is the peak position for the Lorentz oscillator, E is the photon energy, and E_g is the band gap energy defined as the photon energy where $\varepsilon_2 = 0$. Note that this formula is valid only for photon energies greater than the band gap energy. The Eq. (A.1) can be simplified by taking into consideration that ε_2 is proportional to $(E-Eg)^2/E^2$, hence it can be re-written[93,94] as

$$E - E_g \propto \sqrt{\varepsilon_2(E)E^2} = \sqrt{\frac{hc}{2\pi}}\sqrt{\alpha(E)n(E)E} \qquad (A.2)$$

where h is the Planck's constant, c is the speed of light, and n – refractive index. Then from Eq. (A.2), plotting $(hc/2\pi)^{1/2}(\alpha nE)^{1/2}$ versus photon energy (E) allows for the straightforward linear extrapolation of the band gap from the graph.

REFERENCES

[1] S. Takagi, R. Zhang, and M. Takenaka, Microelectron. Eng. **109**, 389 (2013).

[2] A. Toriumi, C.H. Lee, S.K. Wang, T. Tabata, M. Yoshida, D.D. Zhao, T. Nishimura, K. Kita, K. Nagashio, Proc. IEEE IEDM Tech. Dig. **2011**, 646.

[3] M. Caymax, G. Eneman, F. Bellenger, C. Merckling, A. Delabie, G. Wang, R. Loo, E. Simoen, J. Mitard, B. De Jaeger, G. Hellings, K. De Meyer, M. Meuris, and M. Heyns, Proc. IEEE IEDM Tech. Dig. **2009**, 461.

[4] P.C. McIntyre, D. Chi, C.O. Chui, H. Kim, K.I. Seo, K.C. Saraswat, R. Sreenivasan, T. Sugawara, F.S. Aguirre-Testado, and R.M. Wallace, ECS Trans. **3**, 519 (2006).

[5] M. Caymax, S. Van Elshocht, M. Houssa, A. Delabie, T. Conard, M. Meuris, M.M. Heyns, A. Dimoulas, S. Spiga, M. Fanciulli, J.W. Seo, and L.V. Goncharova, Mater. Sci. Eng. B **135**, 256 (2006).

[6] A. Toriumi, T. Tabata, C.H. Lee, T. Nishimura, K. Kita, and K. Nagashio, Microelectron. Eng. **86**, 1571 (2009).

[7] Q. Xie, S. Deng, M. Schaekers, D. Lin, M. Caymax, A. Delabie, X-P. Qu, Y-L. Jiang, D. Deduytsche, and C. Detavernier, Semicond. Sci. Techn. **27**, 074012 (2012).

[8] T. Nishimura, C.H. Lee, S.K. Wang, T. Tabata, K. Kita, K. Nagashio, and A. Toriumi, Proc. IEEE Symp. on VLSI Techn. **2010**, 209.

[9] C.H. Lee, T. Nishimura, T. Tabata, S.K. Wang, K. Nagashio, K. Kita, and A. Toriumi, Proc. IEEE IEDM Tech. Dig. **2010**, 416.

[10] C.H. Lee, T. Nishimura, N. Saido, K. Nagashio, K. Kita, and A. Toriumi, Proc. IEEE IEDM Tech. Dig. **2009**, 457.

[11] C.H. Lee, T. Nishimura, K. Nagashio, K. Kita, A. Toriumi, IEEE Trans. Electron. Dev. **58**(5), 1295 (2011).

[12] A. Delabie, F. Bellenger, M. Houssa, T. Conard, S. V. Elshocht, M. Caymax, M. Heyns, and M. Meuris, Appl. Phys. Lett. **91**, 082904 (2007).

[13] H. Matsubara, T. Sasada, M. Takenaka, and S. Takagi, Appl. Phys. Lett. **93**, 032104 (2008).

[14] Y. Nakakita, R. Nakane, T. Sasada, H. Matsubara, M. Takenaka, and S. Takagi, Proc. IEEE IEDM Tech. Dig. **2008**, 877.

[15] R. Xie, T. H. Phung, W. He, Z. Sun, M. Yu, Z. Cheng, and C. Zhu, Proc. IEEE IEDM Tech. Dig. **2008**, 393.

[16] H.-Y. Yu, M. Ishibashi, J.-H. Park, M. Kobayashi, and K. C. Saraswat, IEEE Electron Device Letters **30**, 675 (2009).

[17] A. Molle, N.K. Bhuiyan, G. Tallarida, and M. Fanciulli, Appl. Phys. Lett. **89**(8), 083504 (2006).

[18] D. Kuzum, P. Jin-Hong, T. Krishnamohan, H-S.P. Wong, K.C. Saraswat, IEEE Trans. Electron. Dev. **58**(4), 1015 (2011).

[19] M. Houssa, G. Pourtois, M. Caymax, M. Meuris, and M. M. Heyns, Appl. Phys. Lett. **92**(24), 242101 (2008).

[20] K. Prabhakaran, F. Maeda, Y. Watanabe, and T. Ogino, Appl. Phys. Lett. **76**(16), 2244 (2000).

[21] T. Takahashi, T. Nishimura, L. Chen, S. Sakata, K. Kita and A. Toriumi, Proc. IEEE IEDM Tech. Dig. **2007**, 697.

[22] C.H. Lee, T. Tabata, T. Nishimura, K. Nagashio, and A. Toriumi, Appl. Phys. Express **2**, 071404 (2009).

[23] Y. Fukuda Y, T. Ueno, S. Hirono, and S. Hashimoto, Japan. J. Appl. Phys. **44**, 6981 (2005).

[24] F. Bellenger,B. De Jaeger, C. Merckling, M. Houssa, J. Penaud, L. Nyns, E. Vrancken, M. Caymax, M. Meuris, T. Hoffmann, K. De Meyer, and M. Heyns, IEEE Electron Device Lett. **31**(5), 402 (2010).

[25] Q. Xie, D. Deduytsche, M. Schaekers, M. Caymax, A. Delabie, X.P. Qu, and C. Detavernier, Electrochem. Solid State Lett. **14**, G20 (2011).

[26] Y. Fukuda, Y. Yazaki, Y. Otani, T. Sato, H. Toyota, and T. Ono, IEEE Trans. Electron Devices **57**, 282 (2010).

[27] K. Kita, S.K. Wang, M. Yoshida, C.H. Lee, K. Nagashio, T. Nishimura, and A. Toriumi, Proc. IEEE IEDM Tech. Dig. **2009**, 693.

[28] R.D. Shannon, J. Appl. Phys. **73**, 348 (1993).

[29] A. Dimoulas, D.P. Brunco, S. Ferrari, J.W. Seo, Y. Panayiotaos, A. Sotiropoulos, T. Conard, M. Caymax, S. Spiga, M. Fanciulli, Ch. Dieker, E.K. Evangelou, S. Galata, M. Houssa, and M.M. Heyns, Thin Solid Films **515**, 6337 (2007).

[30] T. Tabata, C. H. Lee, K. Kita and A. Toriumi, ECS Trans. **16**(5), 479 (2008).

[31] J.J. Gu, Y.Q. Liu, M. Xu, G.K. Celler, R.G. Gordon, P.D. Ye, Appl. Phys. Lett. **97**, 012106 (2010).

[32] K. Kita, K. Kyuno, and A. Toriumi, Appl. Phys. Lett. **85**, 52 (2004).

[33] R. Zhang, T. Iwasaki, N. Taoka, M. Takenaka, and S. Takagi, Proc. IEEE Symp. VLSI Techn. **2011**, 56.

[34] R. Zhang, P.C. Huang, J.C. Lin, M. Takenaka, and S. Takagi, Proc. IEEE IEDM Tech. Dig. **2012**, 371.

[35] R. Zhang, T. Iwasaki, N. Taoka, M. Takenaka, S. Takagi, IEEE Trans. Electron Dev. **59**, 335 (2012).

[36] R. Zhang, T. Iwasaki, N. Taoka, M. Takenaka, and S. Takagi, Appl. Phys. Lett. **98**, 112902 (2011).

[37] R. Zhang, P. C. Huang, N. Taoka, M. Takenaka and S. Takagi, Proc. IEEE Symp. VLSI Techn. **2012**, 161.

[38] E. Dentoni Litta, P-E. Hellström, C. Henkel, and M. Östling, IEEE Trans. Electron Dev. **60**(10), 3271 (2013).

[39] I.Z. Mitrovic, M. Althobaiti, A.D. Weerakkody, N. Sedghi, S. Hall, V.R. Dhanak, P.R. Chalker, C. Henkel, E. Dentoni Litta, P.-E. Hellström, and M. Östling, Microelectron. Eng. **109**, 204 (2013).

[40] K. Kita, T. Takahashi, H. Nomura, S. Suzuki, T. Nishimura, and A. Toriumi, Appl. Surf. Sci. **254**, 6100 (2008).

[41] J. Song, K. Kakushima, P. Ahmet, K. Tsutsui, N. Sugi, T. Hattori, H. Iwai, Microelectron. Eng. **84**, 2336 (2007).

[42] J. Song, K. Kakushima, P. Ahmet, K. Tsutsui, N. Sugii, T. Hattori, and H. Iwai, Jap. J. Appl. Phys. **46**(16), L376 (2007).

[43] G. Mavrou, S.F. Galata, A. Sotiropoulos, P. Tsipas, Y. Panayiotatos, A. Dimoulas, E.K. Evangelou, J. W. Seo, and Ch. Dieker, Microelectron. Eng. **84**, 2324 (2007).

[44] G. Mavrou, S. Galata, P. Tsipas, A. Sotiropoulos, Y. Panayiotatos, A. Dimoulas, E. K. Evangelou, J. W. Seo, and Ch. Dieker, J. Appl. Phys. **103**, 014506 (2008).

[45] C. Rossel, A. Dimoulas, A. Tapponnier, D. Caimi, D. J. Webb, C. Andersson, M. Sousa, C. Marchiori, H. Siegwart, J. Fompeyrine, and R. Germann, Proc. ESSDERC **2008**, 79.

[46] J. Song, K. Kakushima, P. Ahmet, K. Tsutsui, N. Sugii, T. Hattori, and H. Iwai, Microelectron. Eng. **86**, 1638 (2009).

[47] G. Mavrou, P. Tsipas, A. Sotiropoulos, S. Galata, Y. Panayiotatos, A. Dimoulas, C. Marchiori, and J. Fompeyrine, Appl. Phys. Lett. **93**, 212904 (2008).

[48] D. Tsoutsou, Y. Panayiotatos, A. Sotiropoulos, G. Mavrou, E. Golias, S.F. Galata, and A. Dimoulas, J. Appl. Phys. **108**, 064115 (2010).

[49] A. Dimoulas, D. Tsoutsou, Y. Panayiotatos, A. Sotiropoulos, G. Mavrou, S. F. Galata, and E. Golias, Appl. Phys. Lett. **96**, 012902 (2010).

[50] V. V. Afanas'ev, A. Stesmans, G. Mavrou, and A. Dimoulas, Appl. Phys. Lett. **93**, 102115 (2008).

[51] H. Li, L. Lin, J. Robertson, Appl. Phys. Lett. **101**, 052903 (2012).

[52] J. Robertson, B. Falabretti, Materials Science and Engineering B **135**, 267 (2006).

[53] J. Robertson, B. Falabretti, J. Appl. Phys. **100**, 014111 (2006).

[54] C. Andersson, C. Rossel, M. Sousa, D. J. Webb, C. Marchiori, D. Caimi, H. Siegwart, Y. Panayiotatos, A. Dimoulas, and J. Fompeyrine, Microelectron. Eng. **86**, 1635 (2009).

[55] M. Leskelä and M. Ritala, J. Solid State Chem. **171**(1/2), 170 (2003).

[56] Y. Zhao, K. Kita, K. Kyuno, and A. Toriumi, Appl. Phys. Lett. **94**, 042901 (2009).

[57] H. Li, L. Lin, and J. Robertson, Appl. Phys. Lett. **101**, 052903 (2012).

[58] X. Zhao and D. Vanderbilt, Phys. Rev. B Condens. Matter. **65**(7), 075105 (2002).

[59] S. Abermann, O. Bethge, C. Henkel, and E. Bertagnolli, Appl. Phys. Lett. **94**(26), 262904 (2009).

[60] C. Henkel, S. Abermann, O. Bethge, G. Pozzovivo, P. Klang, M. Reiche, and E. Bertagnolli, IEEE Trans. Electron. Dec. **57**(12), 3295 (2010).

[61] C. X. Li and P. T. Laia, Appl. Phys. Lett. **95**, 022910 (2009).

[62] Y-H. Wu, M.L. Wu, R.J. Lyu, J.R. Wu, L.L. Chen, C.C. Lin, Appl. Phys. Lett. **98**, 203502 (2011).

[63] Z.Q. Liu, W.K. Chim, S.Y. Chiam, J.S. Pan, C.M. Ng, Appl. Phys. Lett. **100**, 092110 (2012).

[64] L. K. Chu, W. C. Lee, M. L. Huang, Y. H. Chang, L. T. Tung, C. C. Chang, Y. J. Lee, J. Kwo, and M. Hong, J. Cryst. Growth **311**, 2195 (2009).

[65] Z.Q. Liu, S.Y. Chiam, W.K. Chim, J.S. Pan, and C.M. Ng, J. Electrochem. Soc. **157**, G250 (2010).

[66] S.Y Chiam, W.K. Chim, C. Pi, A.C.H. Huan, S.J. Wang, J.S. Pan, S. Turner, J. Zhang, J. Appl. Phys. **103**, 083702 (2008).

[67] J. Sune, S. Tous, and E. Miranda, Appl. Phys. Lett. **97**, 213503 (2010).

[68] M-L. Wu, Y-H. Wu, R-J. Lyu, C-Y. Chao, C-Y. Wu, C-C. Lin, L-L. Chen, Microelectronic Eng. **109**, 216-9 (2013).

[69] A. Chroneos, A. Dimoulas, J. Appl. Phys. **111**, 023714 (2012).

[70] G. Beamson, D. Briggs, S.F. Davies, I.W. Fletcher, D.T. Clark, J. Howard, U. Gelius, B. Wannberg and P. Balzer, Surf. Interface. Anal. **15**, 541 (1990).

[71] J.C. Vickerman, *Surface analysis* (John Wiley, 1998).

[72] D.A. Shirley, Phys. Rev. B **5**, 4709 (1972).

[73] E. Bersch, M. Di, S. Consiglio, R.D. Clark, G.J. Leusink, A.C. Diebold, J. Appl. Phys. **107**, 043702 (2010).

[74] M. Perego, G. Seguini, J. Appl. Phys. **110**, 053711 (2011).

[75] W.F. Zhang, T. Nishimula, K. Nagashio, K. Kita, A. Toriumi, Appl. Phys. Lett. **102**, 102106 (2013).

[76] S. Baldovino, A. Molle, and M. Fanciulli, Appl. Phys. Lett. **93**, 242105 (2008).

[77] D. Schmeisser, R.D. Schnell, A. Bogen, F.J. Himpsel, D. Rieger, G. Landgren, and J.F. Morar, Surf. Sci. **172**, 455 (1986).

[78] T. Sasada, Y. Nakakita, M. Takenaka, and S. Takagi, J. Appl. Phys. **106**, 073716 (2009).

[79] I.Z. Mitrovic, S. Hall, N. Sedghi, G. Simutis, V.R. Dhanak, P. Bailey, T.C.Q. Noakes, I. Alexandrou, O. Engstrom, J.M.J. Lopes, J. Schubert, J. Appl. Phys. **112**, 044102 (2012).

[80] J.M.J. Lopes, M. Roeckerath, T. Heeg, J. Schubert, U. Littmark, S. Mantl, A. Besmehn, P. Myllymaki, L. Niinisto, C. Adamo, and D.G. Schlom, ECS Trans. **11**(4), 311 (2007).

[81] D. Schmeiser, K. Henkel, M. Bergholz, and M. Tallarida, Superlatt. and Microstruct. **47**, 369 (2010).

[82] M. Perego, G. Scarel, M. Fanciulli, I.L. Fedushkin, and A.A. Skatova, Appl. Phys. Lett. **90**, 162115 (2007).

[83] F.G. Bell, L. Ley, Phys. Rev. B **37**, 8383 (1988).

[84] A. Ohta, H. Nakagawa, H. Murakami, S. Higashi, and S. Miyazaki, Surf. Sci. Nanotech. **4**, 174 (2006).

[85] G.E. Jellison, Jr. and F.A. Modine, Appl. Phys. Lett. **69**, 371 (1996); Erratum, Appl. Phys. Lett. **69**, 2137 (1996).

[86] H.G. Tompkins and E. A. Irene, *Handbook of Ellipsometry* (William Andrew, Norwich, NY, Springer 2006), p. 870.

[87] B. Johs and J.S. Hale, Phys. Stat. Sol. (a) **205**(4), 715 (2008).

[88] J. Price, P.S. Lysaght, S.C. Song, H-J. Li, and A.C. Diebold, Appl. Phys. Lett. **91**, 061925 (2007).

[89] A. Toriumi, S.K. Wang, C.H. Lee, M. Yoshida, K. Kita, T. Nishimura, and K. Nagashio, ECS Trans. **28**(2), 171 (2010).

[90] H. Hosono, Y. Abe, D.L. Kinser, R.A. Weeks, K. Muta and H. Kawazoe, Phys. Rev. B **46**, 11445 (1992).

[91] A.S. Zyubin, A.M. Mebel, and S.H. Lin, J. Chem. Phys. **123**, 044701 (2005).

[92] A.S. Zyubin, A.M. Mebel, and S.H. Lin, J. Chem. Phys. **125**, 064701 (2006).

[93] N. V. Nguyen, A. V. Davydov, D. Chandler-Horowitz, and M. M. Frank, Appl. Phys. Lett. **87**, 192903 (2005).

[94] N. V. Nguyen, S. Sayan, I. Levin, J.R. Ehrstein, I.J.R. Baumvol, C. Driemeier, C. Krug, L. Wielunski, R.Y. Hung, and A. Diebold, J. Vac. Sci. Technol. A **23**, 1706 (2005).

[95] M. Di, E. Bersch, A.C. Diebold, S. Consiglio, R.D. Clark, G.J. Leusink, T. Kaack, J. Vac. Sci. Techn. A **29**(4), 041001 (2011).

[96] J. Robertson, P.W. Peacock, in *Materials fundamentals of gate dielectrics*, eds. A.A. Demkov and A. Navrotsky (Springer, 2005).

[97] S. Zhang, R. Xiao, J. Appl. Phys. **83**(7), 3842 (1998).

[99] A. Ohta, M. Yamaoka, S. Miyazaki, Microelectron. Eng. **72**, 154-9 (2004).

[99] T. Tomiki, J. Tamashiro, Y. Tanahara, A. Yamada, H. Fukutani, T. Miyahara, H. Kato, S. Shin, and M. Ishigame, J. Phys. Soc. Japan **55**(12), 4543 (1986).

[100] V. V. Afanas'ev, M. Houssa, A. Stesmans, and M. M. Heyns, J. Appl. Phys. **91**, 3079 (2002).

[101] V. V. Afanas'ev, A. Stesmans J. Appl. Phys. **102**, 081301 (2007).

[102] H.Y. Yu, M.F. Li, B.J. Cho, C.C. Yeo, M.S. Joo, D.L. Kwong, Appl. Phys. Lett. **81**, 376 (2002).

[103] F. L. Martinez, M. Toledano-Luque, J.J. Gandia, J. Carabe, W. Bohne, J. Rohrich, E. Strub, and I. Martil, J. Phys. D: Appl. Phys. **40**, 5256 (2007).

[104] F. Urbach, Phys. Rev. **92**, 1324 (1953).

[105] Cho Y J, Nguyen N V, Richter C A, Ehrstein J R, Lee B H and Lee J C, Appl. Phys. Lett. **80**, 1249 (2002).

[106] H. Takeuchi, D. Han D and T-J. King, J. Vac. Sci. Technol. A **22**, 1337 (2004).

[107] J. Robertson, Phil. Mag. B **69**, 307 (1994).

[108] Z.Q. Liu, W.K. Chim, S.Y. Chiam, J.S. Pan, and C.M. Ng, J. Appl. Phys. **109** (2011) 093701.
[109] R.L. Opila, G.D. Wilk, M.A. Alam, R.B. van Dover, and B.W. Busch, Appl. Phys. Lett. **81**, 1788 (2002).
[110] T. Nakayama, S. Itaya, and D. Murayama, J. Phys.: Conf. Series **38**, 216 (2006).
[111] S. Y. Chiam, W. K. Chim, A. C. H. Huan, J. S. Pan, and J. Zhang, Appl. Phys. Lett. **88**, 011904 (2006).
[112] Z.Q. Liu, W.K. Chim, S.Y. Chiam, J.S. Pan, S.R. Chun, Q. Liu, C.M. Ng, Surface Science **606**, 1638 (2012).
[113] E. Kraut, R. Grant, J. Waldrop, and S. Kowalczyk, Phys. Rev. Lett. **44**, 1620 (1980).
[114] S.A. Chambers, T. Droubay, T.C. Kaspar, and M. Gutowski, J. Vac. Sci. Techn. B **22**, 2204 (2004).
[115] M. Perego, G. Scarel, M. Fanciulli, I.L. Fedushkin, and A.A. Skatova, Appl. Phys. Lett. **90**, 162115 (2007).
[116] M. Yang, R.Q. Wu, Q. Chen, W.S. Deng, Y.P. Feng, J.W. Chai, J.S. Pan, S.J. Wang, Appl. Phys. Lett. **94**, 142903 (2009).
[117] W.F. Zhang, T. Nishimula, K. Nagashio, K. Kita, and A. Toriumi, Appl. Phys. Lett. **102**, 102106 (2013).
[118] D. P. Norton, Mater. Sci. Eng. R. **43**, 139 (2004).
[119] H. Li, J. Robertson, Microelectronic Eng. **109**, 244 (2013).

TABLE I. Summary of thickness and band gap data determined by MEIS and VUV-VASE. The literature data[39,56,66,97-102] for the band gap of various La_2O_3 and Y_2O_3 films deposited on Ge and Si are added for comparison. (PLD refers to Pulsed Laser Deposition, ALD to Atomic Layer Deposition, and PC to photoconductivity measurement method.)

Sample	Deposition	Thickness (nm)		Band gap (eV)			
		MEIS	VASE	Tauc		α-method	XPS/PC
				$(\alpha nE)^{1/2}$	$(\alpha E)^2$		
La_2O_3/Ge dep. @ 44°C	MBE	2.6	…	…	…	…	…
La_2O_3/Ge dep. @ 400°C	MBE	3.0	…	…	…	…	5.45
La_2O_3/Si[a]	rf sputtering	…	…	…	…	5.3[a]	…
Y_2O_3/Ge dep. @ 225°C	MBE	…	6.3	5.65	5.70	5.99	…
Y_2O_3/Ge dep. @ 400°C	MBE	…	7.9	5.77	5.77	5.99	…
Y_2O_3/Ge[a]	rf sputtering	…	…	…	…	5.7[a]	…
Y_2O_3/Ge[b]	rf sputtering	…	…	…	…	…	5.7[b]
Y_2O_3/Si[c]	PLD	…	…	…	5.60[c]	…	…
Y_2O_3/SiO_2/Si[d]	thermal decomposition	…	…	…	…	…	6.0[d]
Y_2O_3[e]	single crystal	…	…	…	…	6.08	…
GeO_2/Ge	thermal oxidation	…	4.4	5.65[f]	…	5.95[f]	…
Al_2O_3/Ge	MBE	…	9.4	6.12	6.33	6.43	…
Al_2O_3/Si[g,h]	ALD	…	…	…	…	…	…/6.2[g,h]
Al_2O_3/Si[i]	ALD	…	…	…	…	…	6.52[i]
Al_2O_3/GeO_2/Ge	MBE	…	7.8/3.2	…	…	…	…
		…	8.9/7.2	…	…	…	…

[a] Ref. 56
[b] Ref. 66
[c] Ref. 97
[d] Ref. 98
[e] Ref. 99
[f] Ref. 39
[g,h] Refs. 100-101
[i] Ref. 102

Figure captions

FIG. 1. (a) The MEIS yield vs photon energy for the La_2O_3/Ge stacks deposited at 44°C and 400°C. (b) La and Ge depth profiles derived from the experimental data shown in (a).

FIG. 2. (a) Ge 3d XPS core level spectra for La_2O_3/Ge stacks deposited at 44°C, 250°C and 400°C. (b) Angle Resolved-XPS Ge 3d core levels for the stack deposited at 400°C. The fitting shown refers to the doublet of Voigt peaks for GeO_x. Note that the spectra shown in (b) are acquired on a lower resolution instrument; hence the spin-orbit splitting for the Ge $3d^0$ substrate peak cannot be seen. There is evidence of GeO_x presence not only at the interface.

FIG. 3. (a) La 4d and (b) O 1s XPS core level spectra for La_2O_3/Ge stacks deposited at 44°C, 250°C and 400°C. The spectra are taken at the normal incidence angle, TOA = 0°. The inset in bottom part of (b) refers to the TOAs of 35° and 70° revealing the surface and bulk features for the 400°C deposited stack. The deconvolution of the main peak in the inset includes sub-peaks of: La-O-La, La-O-Ge (LGO), La-OH, and Ge-O-Ge from low to high BEs of O 1s peak.

FIG. 4. (a) High resolution valence band spectra for La_2O_3/Ge stacks deposited at 44°C, 250°C and 400°C. (b) O 1s XPS energy loss spectrum for the stack deposited at 400°C showing the band gap value of ~ 5.4 eV. (c) The schematic of the band diagram for La_2O_3/Ge deposited at 400°C.

FIG. 5. Real (a), and imaginary (b) part of dielectric function vs photon energy for Y_2O_3/Ge stacks deposited at 225°C and 400°C. The dielectric function of GeO_2/Ge with and without capping Al_2O_3 layer is added as a reference.

FIG. 6. The absorption coefficient (a) and (c), and Tauc $(\alpha nE)^{1/2}$ (b) and (d) vs photon energy plots for Y_2O_3/Ge (deposited at 225°C and 400°C) and Al_2O_3/Ge gate stacks. The inset in (a) shows logarithmic α vs E plots. The insets in (b) and (d) refer to $(\alpha E)^2$ vs E Tauc plots.

FIG. 7. (a) Ge 3d, (b) Y 3d, and (c) O 1s XPS core levels for Y_2O_3/Ge deposited at 225°C and 400°C, with GeO_2/Ge and pure Y_2O_3 as reference core level spectra; (d) the referring XRD spectra.

FIG. 8. Ge 3d XPS core level for Y_2O_3/Ge deposited at 225°C and 400°C after in-situ anneal from 425°C to 750°C, in steps of 25°C.

FIG. 9. Ge 3d XPS core level fitting after in-situ anneal for two different Y_2O_3/Ge gate stacks deposited at: (a) 225°C, and b) 400°C.

FIG. 10. (a) The XPS spectra for the calculation of VBO for Y_2O_3/Ge using Kraut's method. (b) Valence band spectra for Y_2O_3/Ge gate stacks showing VBO of 2.4 ± 0.20 eV; (c) Derived band diagram for the Y_2O_3/Ge stack.

FIG. 11. Capacitance voltage characteristics for 10 nm (nominal) Y_2O_3/n-Ge gate stacks deposited at (a) 225°C, and (b) 400°C.

FIG. 12. Current density vs voltage characteristics for 10 nm (nominal) Y_2O_3/n-Ge gate stacks deposited at (a) 225°C, and (b) 400°C.

FIG. 13. Ge 3d XPS core levels fitting for the (a) GeO_2/Ge, (b) Al_2O_3/3.2 nm GeO_2/Ge, (c) Al_2O_3/7.2 nm GeO_2/Ge and (d) Al_2O_3/Ge.

FIG. 14. (a) Al 2p and (b) O 1s XPS core level spectra for GeO_2/Ge, with and without Al_2O_3 cap, and Al_2O_3 on Ge.

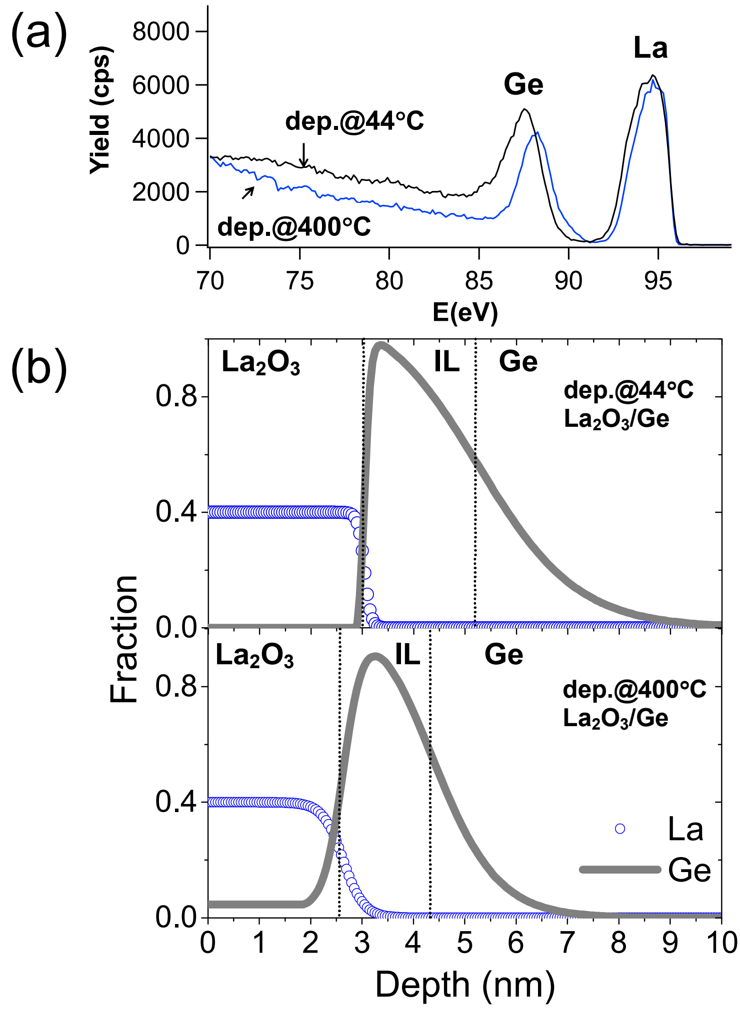

FIG. 1.

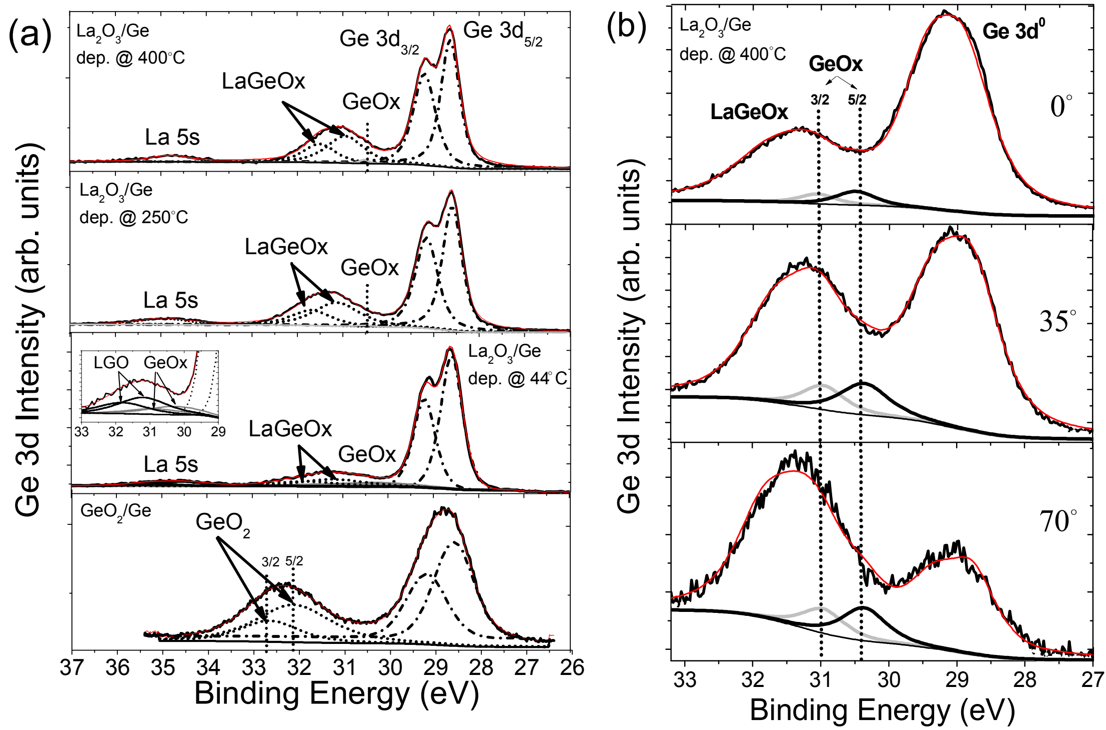

FIG. 2.

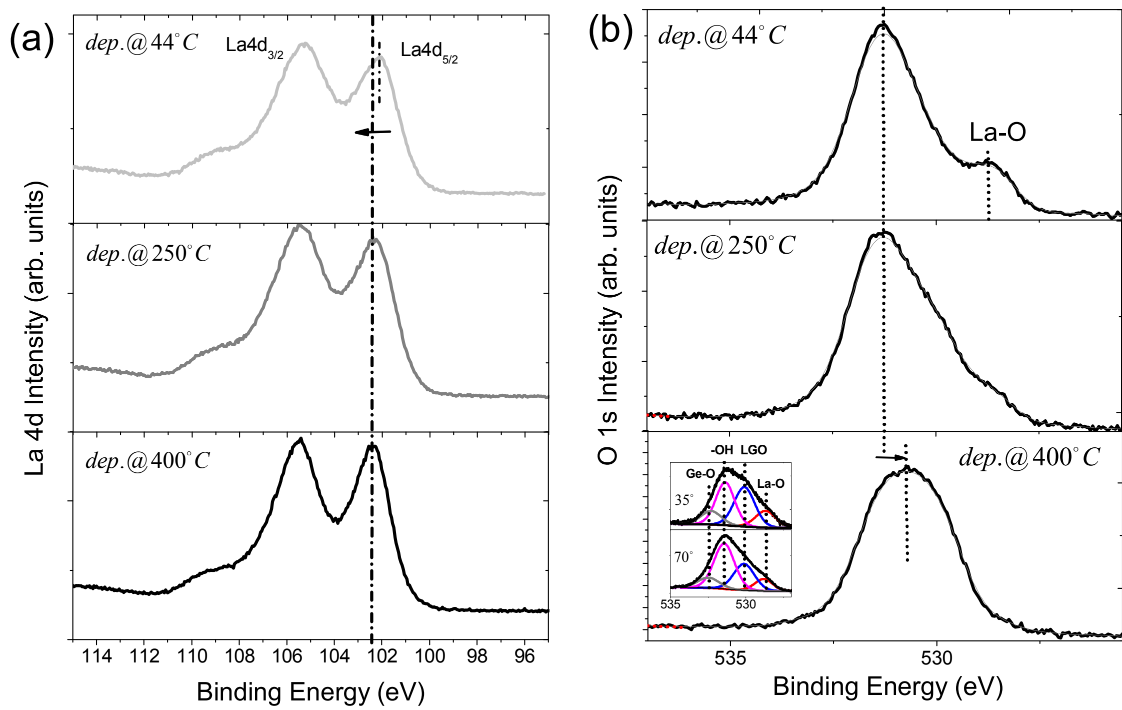

FIG. 3.

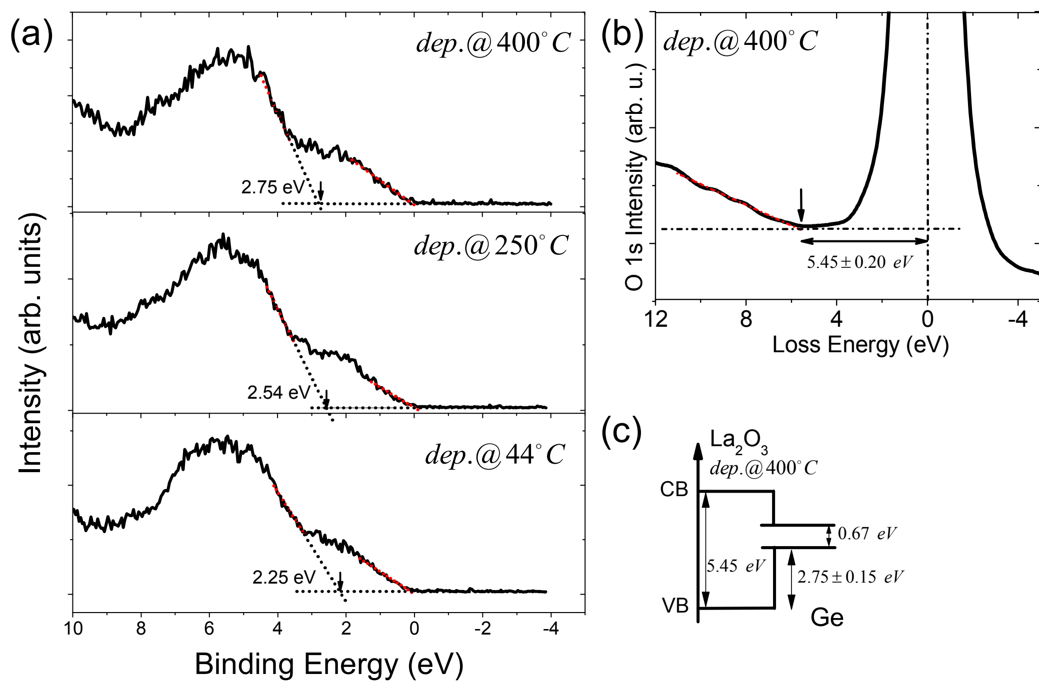

FIG. 4.

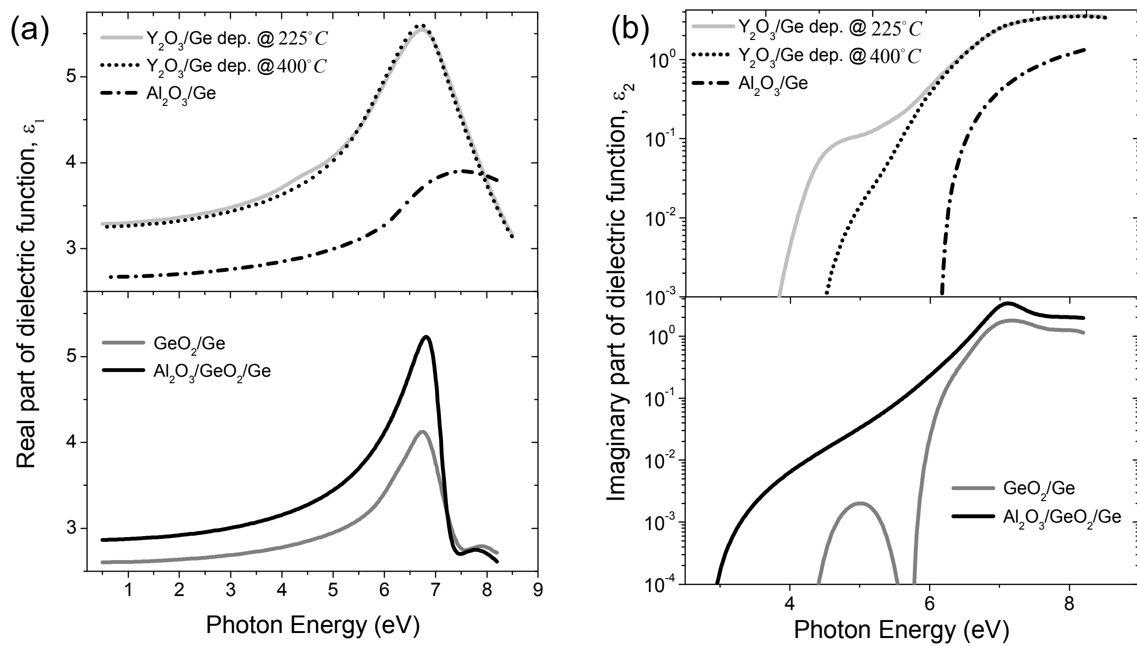

FIG. 5.

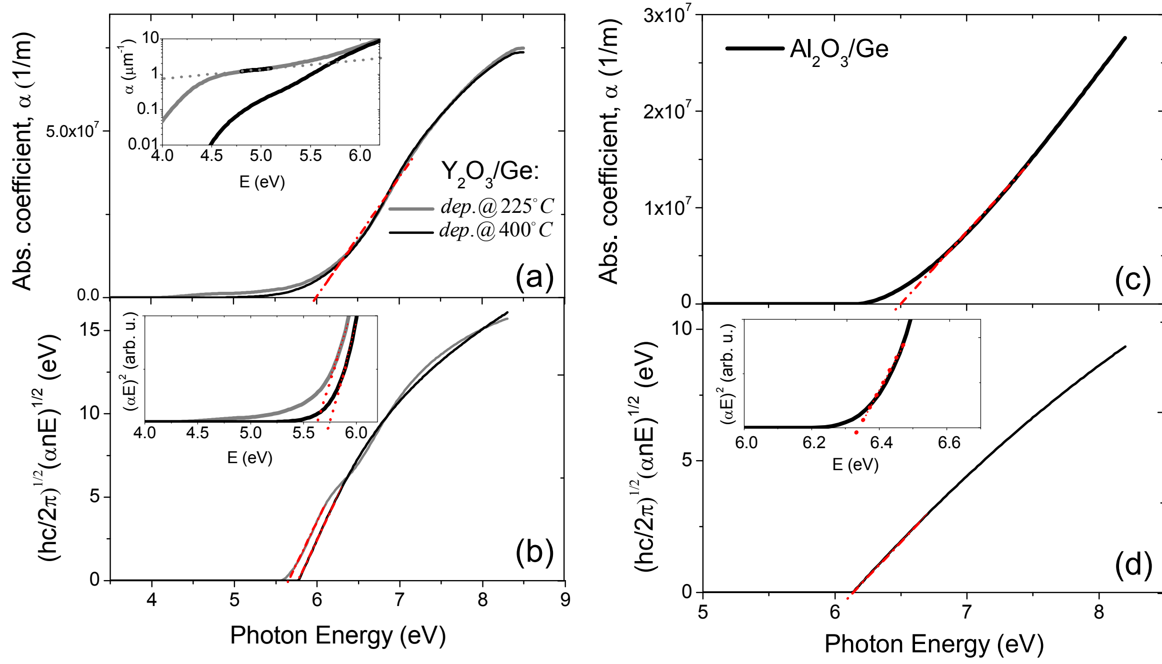

FIG. 6.

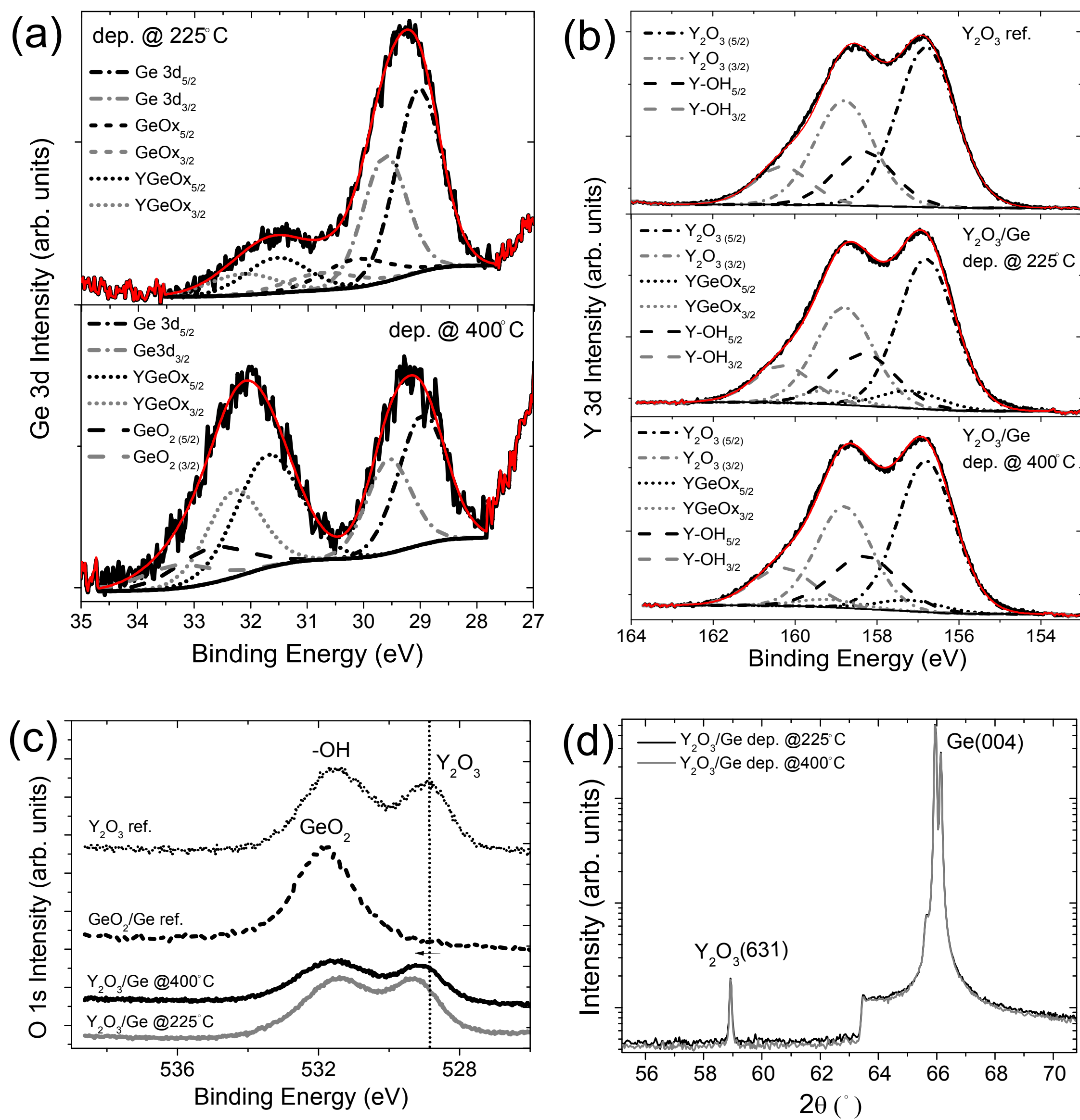

FIG. 7.

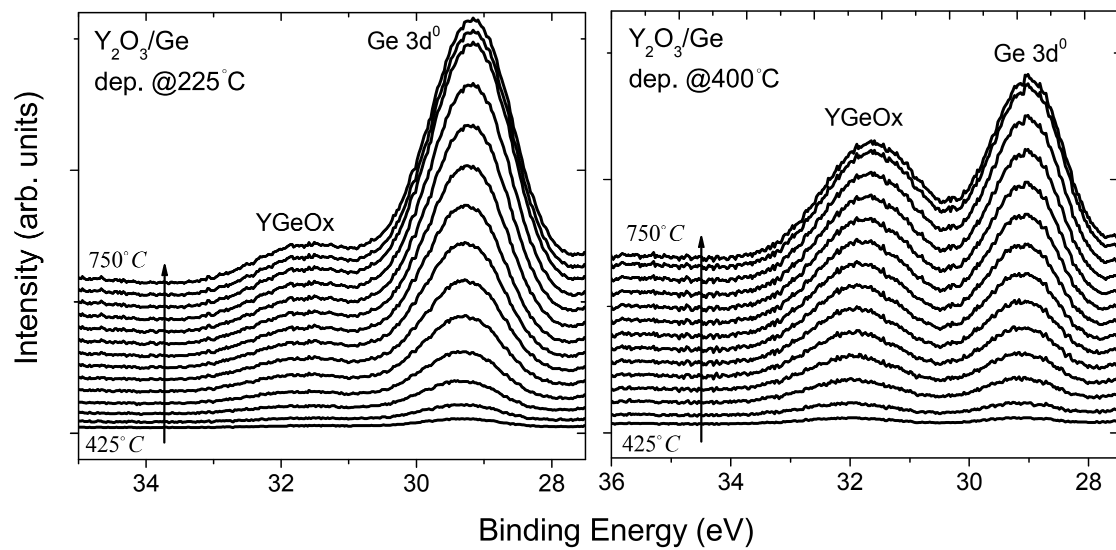

FIG. 8.

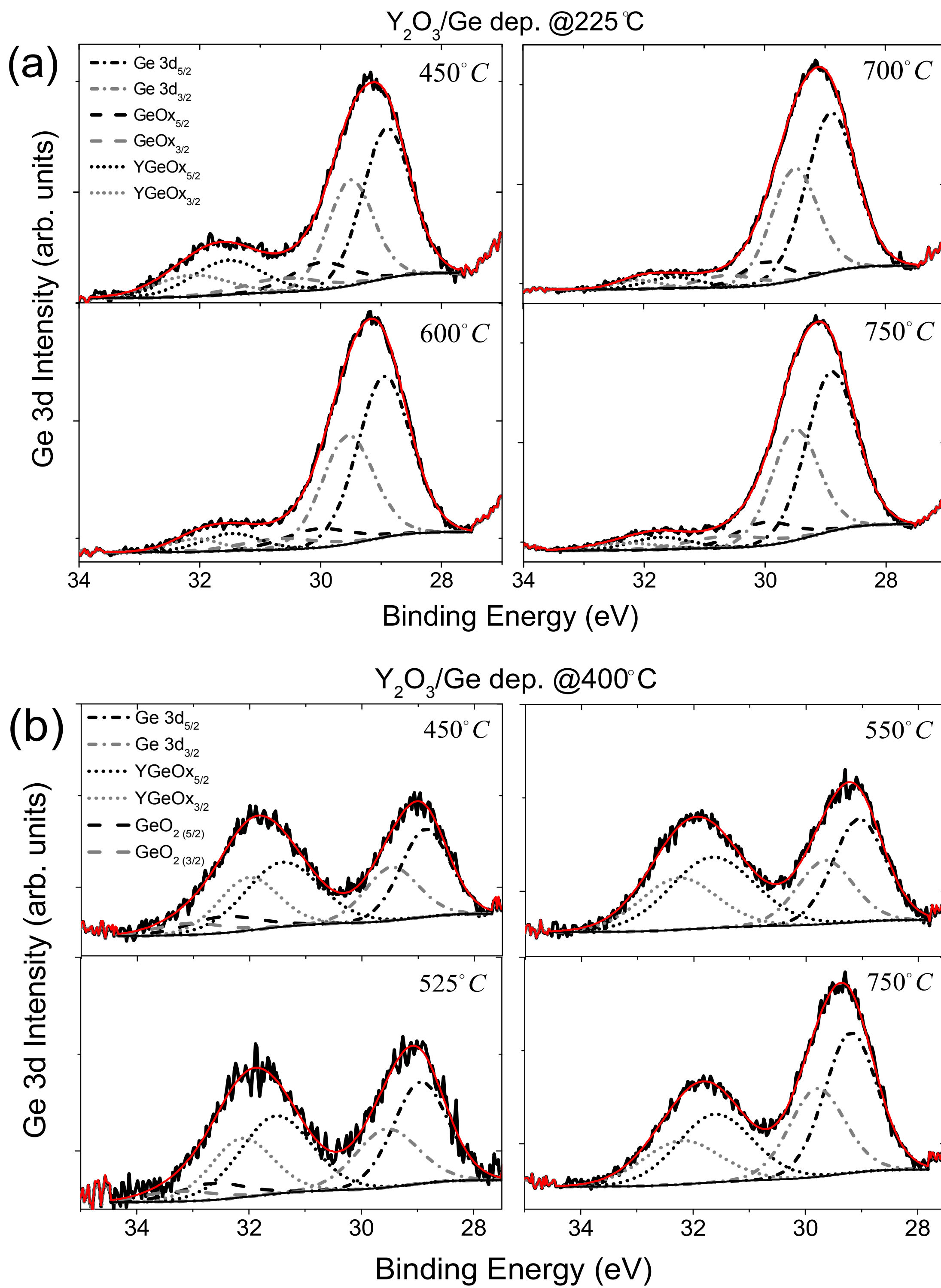

FIG. 9.

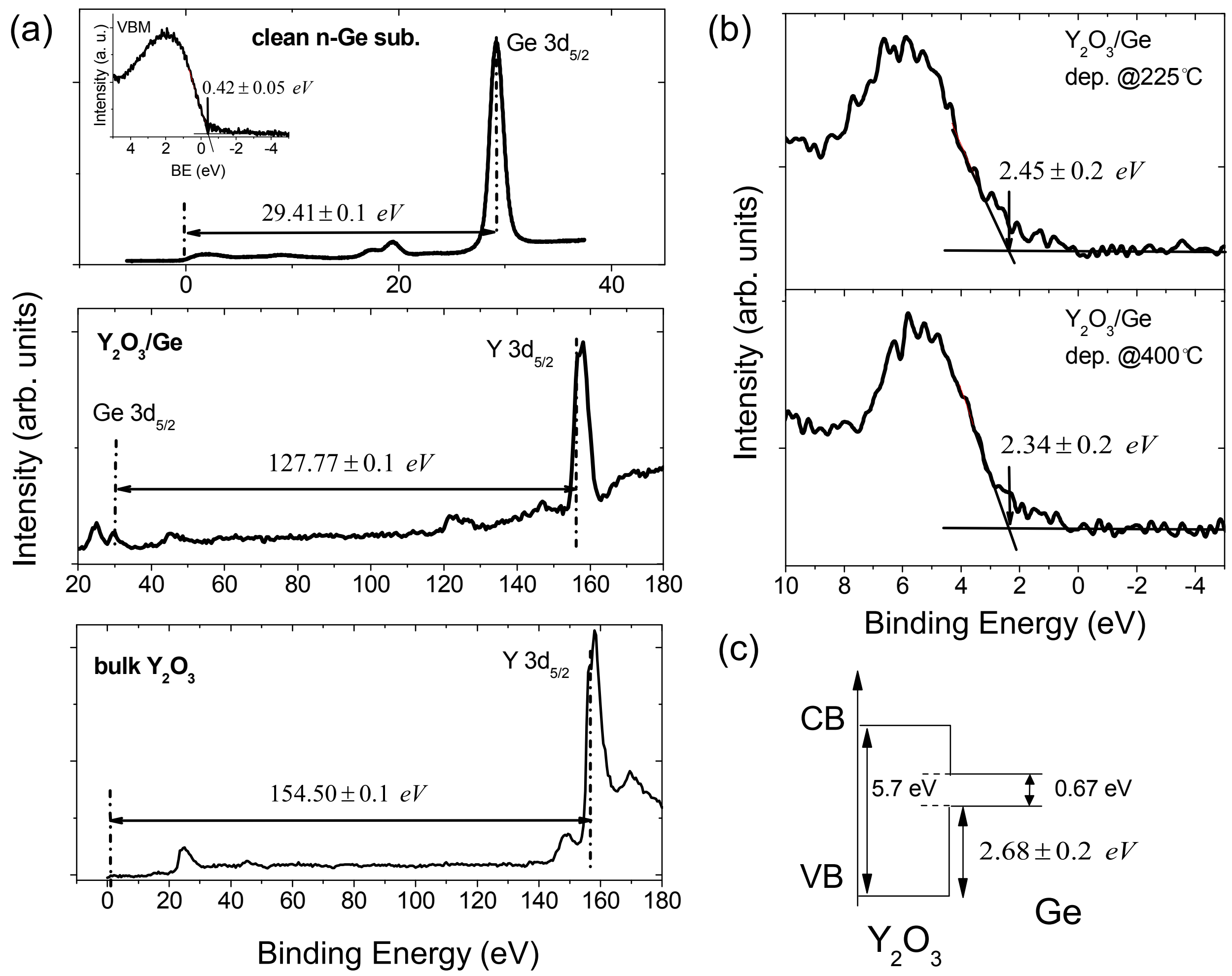

FIG. 10.

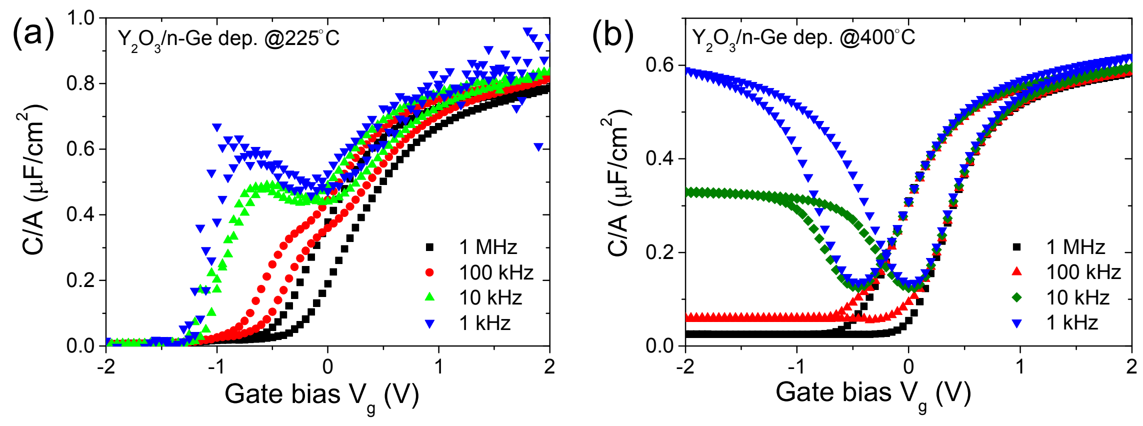

FIG. 11.

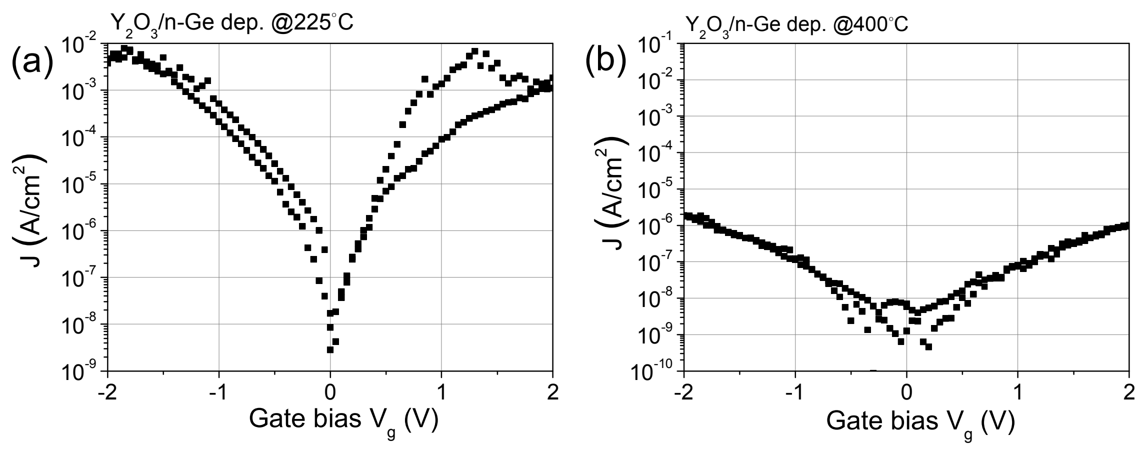

FIG. 12.

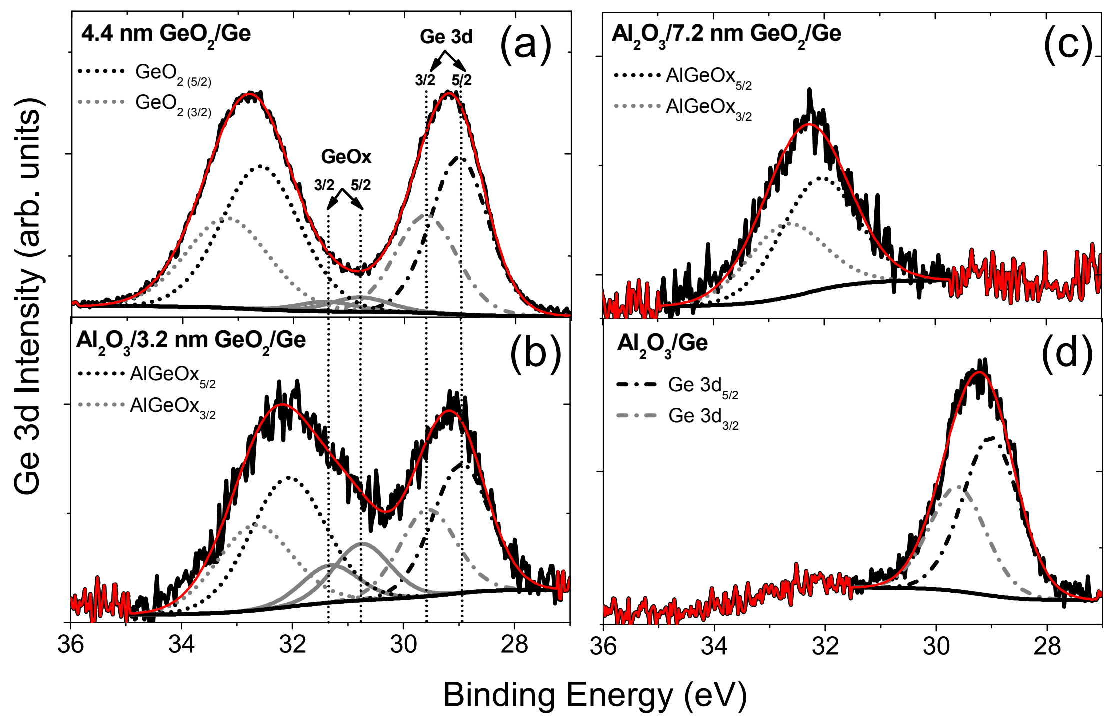

FIG. 13.

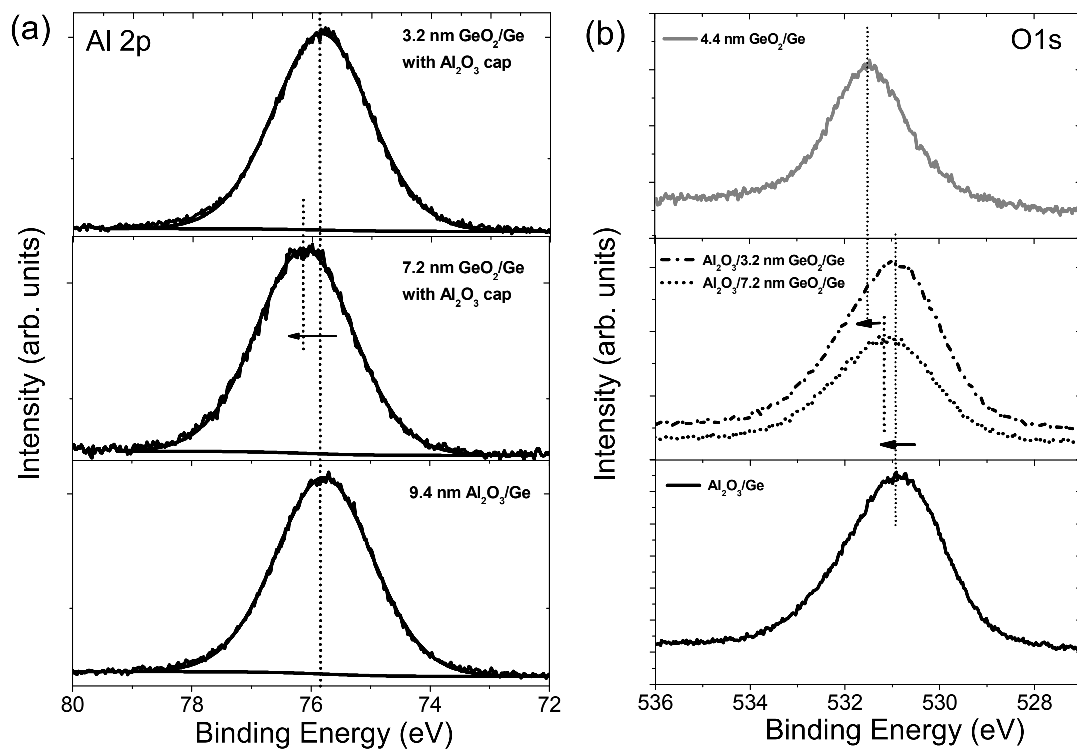

FIG. 14.